

Axial and Vector Structure Functions for Electron- and Neutrino-Nucleon Scattering

Using Effective Leading order Parton Distribution Functions

A. Bodek¹ and Un-ki Yang²

¹ Department of Physics and Astronomy, University of Rochester, Rochester, NY 14627-0171

² Department of Physics and Astronomy, Seoul National University, Seoul 151-747, Korea

Received: date / Revised version: Mar. 15, 2013 version 1.8)

Abstract. We construct a model for inelastic neutrino- and electron-nucleon scattering cross sections using effective leading order parton distribution functions with a new scaling variable ξ_w . Non-perturbative effects are well described using the ξ_w scaling variable, in combination with multiplicative K factors at low Q^2 . Our model describes all inelastic charged lepton-nucleon scattering (including resonance) data (HERA/NMC/BCDMS/SLAC/JLab) ranging from very high Q^2 to very low Q^2 and down to the photo-production region. The model describes existing inelastic neutrino-nucleon scattering measurements, and has been developed to be used in analysis of neutrino oscillation experiments in the few GeV region.

PACS. 13.60.Hb Total and inclusive cross sections (including deep-inelastic processes) – 13.15.+g Neutrino interactions – 13.60.-r Photon and charged-lepton interactions with hadrons

1 Introduction

The field of neutrino oscillation physics has progressed from the discovery of neutrino oscillation [1] to an era of precision measurements of mass splitting and mixing angles. The cross sections for neutrino interactions in the few GeV region are not well known. This results in systematic uncertainties in the extraction of mass splitting and mixing parameters in neutrino oscillations experiments such as MINOS[2,3], NO ν A[4], K2K [5], SuperK[6], T2K[7], and MiniBooNE[8]. A reliable model of neutrino inelastic cross sections at low energies is essential for precise neutrino oscillations experiments.

The renewed interest in neutrino interactions at low energies has resulted in the construction of several near detectors (e.g. MINOS[3], T2K[7]) to measure low energy cross sections and fluxes, as well as experiments (e.g. SciBooNE [9], and MINERvA[10]) which are specifically designed to measure neutrino cross sections at low energies.

In this communication, we report on a duality based model of neutrino interactions using effective leading order parton distribution functions (PDFs). Earlier versions of the model[11,12] have been incorporated into several Monte Carlo generators of neutrino interactions including NEUT[13], GENIE[14], NEUGEN[15] and NUANCE[16].

In the few GeV region, there are contributions from three kinds of neutrino interaction processes as defined by the final state invariant mass W . These include quasi-elastic reactions ($W < 1.07$ GeV/c²), resonance production (e.g. the $\Delta(1232)$ region $1.1 < W < 1.4$ GeV/c² and

higher mass resonances with $1.4 < W < 2.0$ GeV/c²), and deep inelastic scattering ($W > 2.0$ GeV/c²). It is quite challenging to disentangle each of those contributions separately, and in particular the contribution of resonance production and inelastic scattering continuum. At low Q^2 there are large non-perturbative contributions to the inelastic cross section. These include kinematic target mass corrections, dynamic higher twist effects, and higher order Quantum Chromodynamic (QCD) terms, and nuclear effects on nuclear targets.

In our previous studies [17–19], non-perturbative effects were investigated within Leading Order (LO), Next-to-Leading Order (NLO) and Next-to-Next Leading Order (NNLO) QCD using charged lepton-nucleon scattering experimental data [20–22]. We found that in NLO QCD, most of the empirical higher-twist terms needed to obtain good agreement with the low energy data for $Q^2 > 1$ (GeV/c)² originate primarily from target mass effects and the missing NNLO terms (i.e. not from interactions with spectator quarks). If such is the case, then these terms should be the same in charged leptons (e, μ) and neutrino (ν_μ) scattering. Therefore, low energy ν_μ data can be described by effective Parton Distribution Functions (PDFs) which are fit to high Q^2 charged lepton-nucleon scattering data, but modified to include target mass and higher-twist corrections that are extracted from low energy e/μ scattering data. For $Q^2 < 1$ (GeV/c)² additional corrections for non-perturbative effects from spectator quarks are required. These corrections can be parametrized as multi-

plicative K factors. Basically, for the charged current neutrino interaction the K factor terms should be the same in ν_μ and e/μ scattering.

Therefore, a model that describes electron and muon scattering can also be used to model neutrino scattering. However, at low Q^2 the vector and axial structure functions may not be same, though they are expected to be the same at high Q^2 . The axial structure functions at very low values of Q^2 are not constrained by muon and electron scattering data.

2 Electron-nucleon and muon-nucleon scattering

In this section we define the kinematic variables for the case of charged lepton scattering from neutrons and protons. The differential cross section for scattering of an unpolarized charged lepton with an incident energy E_0 , final energy E' and scattering angle θ can be written in terms of the structure functions \mathcal{F}_1 and \mathcal{F}_2 as:

$$\frac{d^2\sigma}{d\Omega dE'}(E_0, E', \theta) = \frac{4\alpha^2 E'^2}{Q^4} \cos^2(\theta/2) \times [\mathcal{F}_2(x, Q^2)/\nu + 2 \tan^2(\theta/2) \mathcal{F}_1(x, Q^2)/M]$$

where α is the fine structure constant, M is the nucleon mass, $\nu = E_0 - E'$ is energy of the virtual photon which mediates the interaction, $Q^2 = 4E_0 E' \sin^2(\theta/2)$ is the invariant four-momentum transfer squared, and $x = Q^2/2M\nu$ is a measure of the longitudinal momentum carried by the struck partons.

Alternatively, one could view this scattering process as virtual photon absorption. Unlike the real photon, the virtual photon can have two modes of polarization. In terms of the cross section for the absorption of transverse (σ_T) and longitudinal (σ_L) virtual photons, the differential cross section can be written as,

$$\frac{d^2\sigma}{d\Omega dE'} = \Gamma [\sigma_T(x, Q^2) + \epsilon \sigma_L(x, Q^2)] \quad (1)$$

where,

$$\Gamma = \frac{\alpha K E'}{4\pi^2 Q^2 E_0} \left(\frac{2}{1 - \epsilon} \right) \quad (2)$$

$$\epsilon = \left[1 + 2 \left(1 + \frac{Q^2}{4M^2 x^2} \right) \tan^2 \frac{\theta}{2} \right]^{-1} \quad (3)$$

$$K = \frac{Q^2(1 - x)}{2Mx}. \quad (4)$$

The quantities Γ and ϵ represent the flux and the degree of longitudinal polarization of the virtual photons respectively. The quantity \mathcal{R} , is defined as the ratio σ_L/σ_T , and is related to the structure functions by,

$$\mathcal{R}(x, Q^2) = \frac{\sigma_L}{\sigma_T} = \frac{\mathcal{F}_2}{2x\mathcal{F}_1} \left(1 + \frac{4M^2 x^2}{Q^2} \right) - 1 = \frac{\mathcal{F}_L}{2x\mathcal{F}_1} \quad (5)$$

where \mathcal{F}_L is called the longitudinal structure function. The structure functions are expressed in terms of σ_L and σ_T as follows:

$$\mathcal{F}_1 = \frac{MK}{4\pi^2 \alpha} \sigma_T, \quad (6)$$

$$\mathcal{F}_2 = \frac{\nu K (\sigma_L + \sigma_T)}{4\pi^2 \alpha (1 + \frac{Q^2}{4M^2 x^2})} \quad (7)$$

$$\mathcal{F}_L(x, Q^2) = \mathcal{F}_2 \left(1 + \frac{4M^2 x^2}{Q^2} \right) - 2x\mathcal{F}_1 \quad (8)$$

or,

$$2x\mathcal{F}_1 = \mathcal{F}_2 \left(1 + \frac{4M^2 x^2}{Q^2} \right) - \mathcal{F}_L(x, Q^2). \quad (9)$$

In addition, $2x\mathcal{F}_1$ is given by

$$2x\mathcal{F}_1(x, Q^2) = \mathcal{F}_2(x, Q^2) \frac{1 + 4M^2 x^2/Q^2}{1 + \mathcal{R}(x, Q^2)}. \quad (10)$$

Standard PDFs are extracted from global fits to various sets of deep inelastic (DIS) scattering data at high energies and high Q^2 , where non-perturbative QCD effects are negligible. PDF fits are performed within the framework of QCD in either LO, NLO or NNLO. Here, using a new scaling variable (ξ_w) we construct effective LO PDFs that account for the contributions from target mass corrections, non-perturbative QCD effects, and higher order QCD terms.

3 The basic model: First iteration with GRV98 PDFs.

Our proposed scaling variable, ξ_w is derived as follows. Using energy momentum conservation, the fractional momentum, ξ carried by a quark in a proton target of mass M is

$$\xi = \frac{2xQ'^2}{Q^2(1 + \sqrt{1 + 4M^2 x^2/Q^2})}, \quad (11)$$

where

$$2Q'^2 = [Q^2 + M_f^2 - M_i^2] + \sqrt{(Q^2 + M_f^2 - M_i^2)^2 + 4Q^2(M_i^2 + P_T^2)}$$

Here M_i is the initial quark mass with average initial transverse momentum P_T , and M_f is the mass of the final state quark. This expression for ξ was previously derived [23] for the case of quark $P_T = 0$.

Assuming $M_i = 0$ we construct following scaling variable

$$\xi_w = \frac{2x(Q^2 + M_f^2 + B)}{Q^2[1 + \sqrt{1 + 4M^2 x^2/Q^2}] + 2Ax}, \quad (12)$$

or alternatively

$$\xi_w = \frac{(Q^2 + M_f^2 + B)}{M\nu[1 + \sqrt{1 + Q^2/\nu^2}] + A}, \quad (13)$$

where in general $M_f = 0$, except for the case of charm-production in neutrino scattering for which we use $M_f = 1.32 \text{ (GeV/c)}^2$.

The parameter A is used to account (on average) for the higher order QCD terms and dynamic higher twist in the form of an enhanced target mass term (the effects of the proton target mass is already taken into account in the denominator of ξ_w). The parameter B is used to account (on average) for the initial state quark transverse momentum (P_T), and also for the effective mass of the final state quark originating from multi-gluon emission. A non-zero B also allows us to describe data in the photoproduction limit (all the way down to $Q^2=0$).

If $A = 0$ and $B = 0$ and $M_f = 0$ then ξ_w is equal to the target mass scaling variable ξ_{TM} where,

$$\xi_{TM} = \frac{Q^2}{M\nu[1 + \sqrt{1 + Q^2/\nu^2}]}, \quad (14)$$

In leading order QCD (e.g. GRV98 PDFs), $\mathcal{F}_{2,LO}$ for the scattering of electrons and muons on proton (or neutron) targets is given by the sum of quark and anti-quark distributions (where each is weighted the square of the quark charges):

$$\mathcal{F}_{2,LO}^{e/\mu}(x, Q^2) = \sum_i e_i^2 [xq_i(x, Q^2) + x\bar{q}_i(x, Q^2)]. \quad (15)$$

Our proposed effective LO PDFs model includes the following:

1. The GRV98 [24] LO Parton Distribution Functions (PDFs) are used to describe $\mathcal{F}_{2,LO}^{e/\mu}(x, Q^2)$. The minimum Q^2 value for these PDFs is 0.8 (GeV/c)^2 .
2. The scaling variable x is replaced with the scaling variable ξ_w as defined in Eq. 12. Here,

$$\begin{aligned} \mathcal{F}_{2,LO}^{e/\mu}(x, Q^2) &= \sum_i e_i^2 \\ &\times [\xi_w q_i(\xi_w, Q^2) + \xi_w \bar{q}_i(\xi_w, Q^2)]. \end{aligned} \quad (16)$$

3. As done in earlier non-QCD based fits [25–28] to low energy charged lepton scattering data, we multiply all PDFs by vector K factors such that they have the correct form in the low Q^2 photo-production limit. Here we use different forms for the sea and valence quarks, separately;

$$\begin{aligned} K_{sea}^{vector}(Q^2) &= \frac{Q^2}{Q^2 + C_s} \\ K_{valence}^{vector}(Q^2) &= [1 - G_D^2(Q^2)] \\ &\times \left(\frac{Q^2 + C_{v2}}{Q^2 + C_{v1}} \right) \end{aligned} \quad (17)$$

where $G_D = 1/(1 + Q^2/0.71)^2$ is the proton elastic form factor. This form of the K factor for valence quarks is motivated by the closure arguments [29] and the Adler [30,31] sum rule. At low Q^2 , $[1 - G_D^2(Q^2)]$ is approximately $Q^2/(Q^2 + 0.178)$, which is close to our earlier fit result [11].

A	B	C_{v1}	C_{v2}	χ^2/ndf
0.419	0.223	0.554	0.431	1235/1200
C_{sea}			N	$\mathcal{F}_{valence}$
0.380			1.011	$[1 - G_D^2(Q^2)]$

Table 1. First iteration with GRV98 PDFs: vector parameters. Only inelastic electron and muon scattering on hydrogen and deuterium (in the continuum region $W > 2 \text{ GeV/c}^2$) are used in the fit. Here the parameters are in units of $(\text{GeV/c})^2$.

These modifications are included in order to describe low Q^2 data in the photoproduction limit ($Q^2=0$), where $\mathcal{F}_2^{e/\mu}(x, Q^2)$ is related to the photoproduction cross section according to

$$\begin{aligned} \sigma(\gamma p) &= \frac{4\pi^2\alpha}{Q^2} \mathcal{F}_2^{e/\mu}(x, Q^2) \\ &= \frac{0.112 \text{ mb}}{Q^2} \mathcal{F}_2^{e/\mu}(x, Q^2) \end{aligned} \quad (18)$$

4. We freeze the evolution of the GRV98 PDFs at a value of $Q^2 = 0.80 \text{ (GeV/c)}^2$. Below this Q^2 , \mathcal{F}_2 is given by;

$$\begin{aligned} \mathcal{F}_2^{e/\mu}(x, Q^2 < 0.8) &= \\ K_{valence}^{vector}(Q^2) \mathcal{F}_{2,LO}^{valence}(\xi_w, Q^2 = 0.8) \\ + K_{sea}^{vector}(Q^2) \mathcal{F}_{2,LO}^{sea}(\xi_w, Q^2 = 0.8) \end{aligned} \quad (19)$$

5. Finally, we fit for the parameters of the modified effective GRV98 LO PDFs (e.g. ξ_w) to inelastic charged lepton scattering data on hydrogen and deuterium targets (SLAC[20]/BCDMS[21]/NMC[22]/H1[32]. In this first iteration, only data with an invariant final state mass $W > 2 \text{ GeV/c}^2$ are included, where $W^2 = M^2 + 2M\nu - Q^2$.

We obtain an excellent fit with the following initial parameters: $A=0.419$, $B=0.223$, and $C_{v1}=0.544$, $C_{v2}=0.431$, and $C_{sea}=0.380$, with $\chi^2/DOF = 1235/1200$. Because of these additional K factors, we find that the GRV98 PDFs need to be scaled up by a normalization factor $N=1.011$. Here the parameters are in units of $(\text{GeV/c})^2$. These parameters are summarised in Table 1.

Thus, in our first iteration we modify the GRV98 \mathcal{F}_2 to describe low energy data down to photo-production limit as follows:

$$\begin{aligned} \mathcal{F}_2^{e/\mu}(x, Q^2) &= \frac{Q^2}{Q^2 + 0.380} \mathcal{F}_{2,LO}^{sea}(\xi_w, Q^2) \\ &+ (1 - G_D^2) \frac{Q^2 + 0.431}{Q^2 + 0.544} \mathcal{F}_{2,LO}^{valence}(\xi_w, Q^2), \end{aligned} \quad (20)$$

where $\xi_w = \frac{2x(Q^2 + 0.223)}{Q^2[1 + \sqrt{1 + 4M^2x^2/Q^2}] + 2 \times 0.419x}$.

In fitting for the effective LO PDFs, the structure functions data are corrected for the relative normalizations between the SLAC, BCDMS, NMC and H1 data (which are allowed to float within the quoted normalization errors). A systematic error shift is applied to the BCDMS data to

account for the uncertainty in their magnetic field, as described in the BCDMS publication[21]. All deuterium data are corrected with a small correction for nuclear binding effects [17–19] as described in section 12. We also include a separate additional charm production contribution using the photon-gluon fusion model in order to fit the very high energy HERA data. This contribution is not necessary for any of the low energy comparisons, but is necessary to describe the very high energy low Q^2 HERA \mathcal{F}_2 and photoproduction data. The charm contribution must be added separately because the GRV98 PDFs do not include a charm sea. Alternatively, one may use a charm sea parametrization from another PDF.

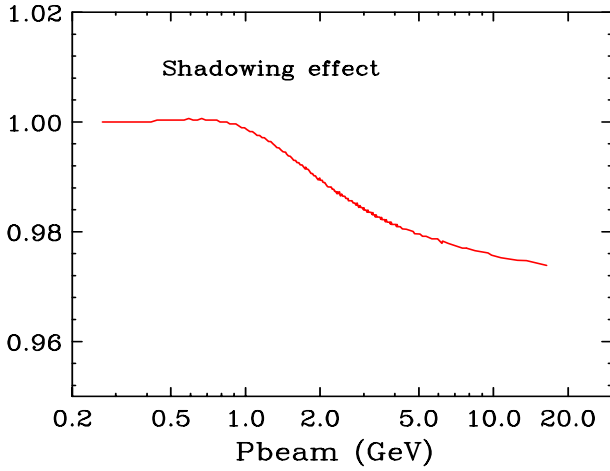


Fig. 1. The ratio of photoproduction cross sections on deuterium to the sum of the photoproduction cross sections on unbound protons and neutrons. This shadowing correction is used to extract the photoproduction cross section on free neutrons and protons.

The first iteration fit successfully describes all inelastic electron and muon scattering data in the continuum region including the very high and very low Q^2 regions. We find that although photo-production data were not included in our first iteration fit, the predictions of our model for the photo-production cross sections on protons and deuterons ($Q^2 = 0$ limit) are also in good agreement with photoproduction measurements[33].

Furthermore, although no resonance data were included in the first iteration fit, the fit also provides a reasonable description of the average value of \mathcal{F}_2 for SLAC and Jefferson data in the resonance region [34] (down to $Q^2 = 0.07$ $(\text{GeV}/c)^2$).

4 Second iteration with GRV98: Including photo-production data, resonances, and additional parameters

We now describe the second iteration of the fit [12]. Theoretically, the K_i factors in Eq. 17 are not required to be

A	B	C_{v2d}	C_{v2u}
0.621	0.380	0.323	0.264
C_{sea}^{down}	C_{sea}^{up}	C_{v1d}	C_{v1u}
0.561	0.369	0.341	0.417
$C_{sea}^{strange}$	$C^{low-\nu}$	$\mathcal{F}_{valence}$	N
0.561	0.218	$[1 - G_D^2(Q^2)]$	1.026

Table 2. Second iteration with GRV98 PDFs: Vector Parameters. Here, we also include photoproduction data on hydrogen and deuterium. No neutrino data are included in the fit. When applicable, all parameters are in units of $(\text{GeV}/c)^2$.

the same for the u and d valence quarks or for the u , d , s , sea quarks and antiquarks. In order to allow flexibility in our effective LO model, we treat the K_i factors for u and d valence and for sea quarks and antiquarks separately.

In this second iteration, in order to get additional constraints on the different K_i factors for up and down quarks separately, we include photo-production data above the $\Delta(1232)$ ($\nu > 1 \text{ GeV}$) for both hydrogen and deuterium. We do not include electron scattering data in the resonance region (on hydrogen and deuterium) in the fit. In order to extract neutron cross section from photoproduction cross sections on deuterium, we apply a small shadowing correction[33] as shown in figure 1. The small nuclear binding corrections for the inelastic lepton scattering data on deuterium is described in section 9.

$$\begin{aligned}
 K^{LW} &= \frac{\nu^2 + C^{low-\nu}}{\nu^2} \quad (W > 1.4 \text{ GeV}/c^2) \\
 K_{sea-strange}^{vector}(Q^2) &= \frac{Q^2}{Q^2 + C_{sea-strange}} \\
 K_{sea-up}^{vector}(Q^2) &= \frac{Q^2}{Q^2 + C_{sea}^{up}} \\
 K_{sea-down}^{vector}(Q^2) &= \frac{Q^2}{Q^2 + C_{sea}^{down}} \\
 K_{valence-up}^{vector}(Q^2) &= K^{LW} [1 - G_D^2(Q^2)] \\
 &\quad \times \left(\frac{Q^2 + C_{v2u}}{Q^2 + C_{v1u}} \right) \\
 K_{valence-down}^{vector}(Q^2) &= K^{LW} ([1 - G_D^2(Q^2)] \\
 &\quad \times \left(\frac{Q^2 + C_{v2d}}{Q^2 + C_{v1d}} \right) \quad (21)
 \end{aligned}$$

The best fit is given by $A = 0.621 \pm 0.009$, $B = 0.380 \pm 0.004$, $C_{v1d} = 0.341 \pm 0.007$, $C_{v1u} = 0.417 \pm 0.024$, $C_{v2d} = 0.323 \pm 0.051$, $C_{v2u} = 0.264 \pm 0.015$, and an $C^{low-\nu} = 0.218 \pm 0.015$ for both down and up quarks.

The sea vector parameters are $C_{sea}^{down} = 0.561$, $C_{sea}^{up} = 0.369$, and $C_{sea}^{strange}$ is set to be the same as C_{sea}^{down} . Here, the parameters are in units of $(\text{GeV}/c)^2$. The fit yields a χ^2/DOF of 2357/1717, and $N = 1.026 \pm 0.003$. The photo-production resonance data (above the $\Delta(1232)$) add to the χ^2/ndf because the fit only provides a smooth average over the higher resonances. No neutrino data are included in the fit. These parameters are summarized in Table 2.

The normalization of the various experiments are allowed to float within their errors with the normalization of the SLAC proton data set to 1.0. The fit yields normalization factors of 0.986 ± 0.002 , 0.979 ± 0.003 , 0.998 ± 0.003 , 1.008 ± 0.003 , 1.001 ± 0.004 , and 0.987 ± 0.005 for the SLAC deuterium data, BCDMS proton data, BCDMS deuterium data, NMC proton data, NMC deuterium data, and H1 proton data, respectively. With these normalization, the GRV98 PDFs with our modifications should be multiplied by $N = 1.026 \pm 0.003$.

Note that we apply a small d/u correction to the GRV98 PDFs. This correction increases the valence d quark distribution at large x and is extracted from NMC data for $\mathcal{F}_2^D/\mathcal{F}_2^P$.

Comparisons of our fit to various sets of inelastic electron and muon \mathcal{F}_2 data on proton and deuteron targets are shown in Figures 2 (for SLAC, BCDMS and NMC). Comparisons to H1(electron-proton) data at low values of x are shown in Figure 3. Our effective LO model describes the inelastic charged lepton \mathcal{F}_2 data both in the low x as well as in the high x regions. The model also provides a very good description of both low energy and high energy photo-production cross sections[33] on proton and deuteron targets for incident photon energies above $\nu = 1$ GeV (which corresponds $W > 1.7$ GeV) as shown in Figure 4. For $W < 1.7$ GeV, as discussed in the next section, the model describes the average cross section over the resonance region.

As seen in the figures our fit describes all of the data, including photo-production data in the continuum region.

5 Comparison to resonance production data

Comparisons of the model fit to hydrogen and deuterium electron scattering data in the resonance region [34] are shown in Figure 5. As expected from quark-hadron duality [35], our model provides a reasonable description of both the inelastic region as well as the average value of the \mathcal{F}_2 data in the resonance region (down to $Q^2 = 0$), including the region of the first resonance ($W = 1.23$ GeV/ c^2). We find also good agreement with the most recent \mathcal{F}_L and \mathcal{F}_2 data in the resonance region from the E94-110, and JUPITER experiments [34,36] at Jlab, as shown in Fig. 6. Our predictions for \mathcal{F}_L are obtained using our \mathcal{F}_2 model and the R_{1998} [37] parametrization (as discussed in section 9). We find good agreement with quark hadron duality down to very low Q^2 . Other studies[31] with unmodified GRV PDFs find large deviations from quark-hadron duality in the resonance region for electron and muon scattering. This is because those studies do not include any low Q^2 K factors and use the scaling variable ξ (while we use the modified scaling variable ξ_w). We find that quark hadron duality works at low Q^2 if we use the modified scaling variable ξ_w , and low Q^2 K_i factors.

In the $Q^2 = 0$ photoproduction limit, the model provides a good descriptions of the data for both the inelastic region as well as in the resonance region as shown in Figure 4.

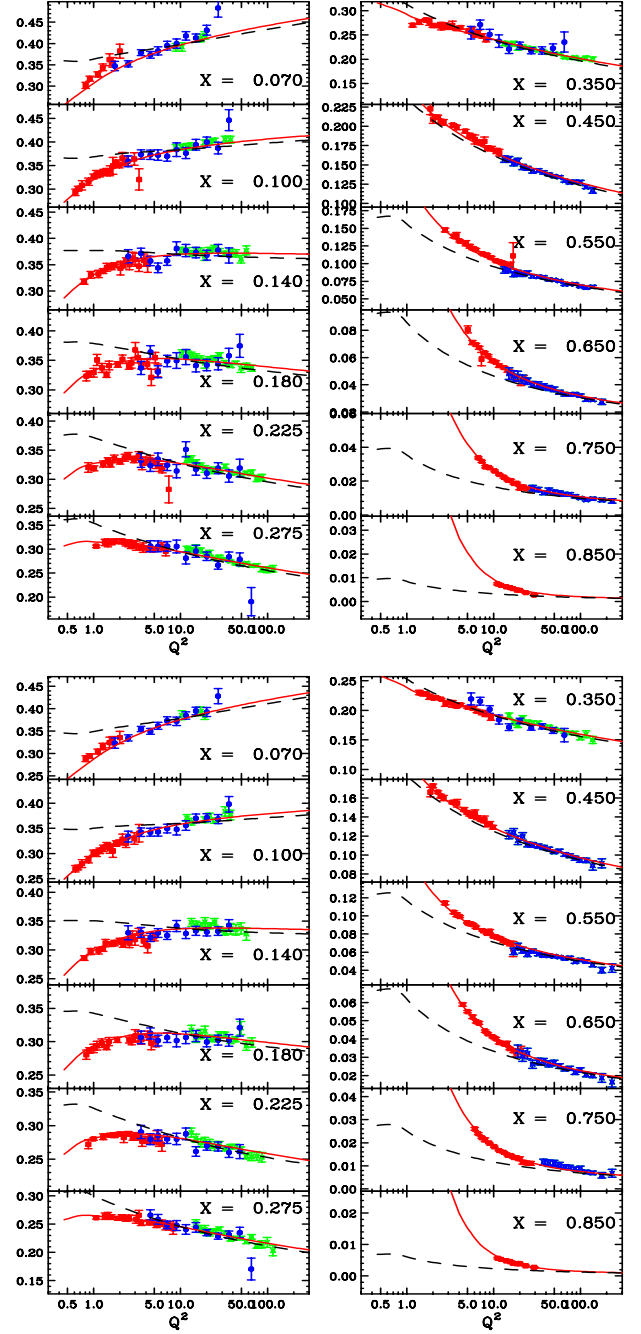


Fig. 2. The effective LO PDF model compared to charged lepton \mathcal{F}_2 experimental data (SLAC, BCDMS, NMC) at high x (these data are included in our fit) :[top] \mathcal{F}_2 proton, [bot] \mathcal{F}_2 deuteron. The solid lines are our fit, and the dashed lines are GRV98 .

6 Application to neutrino scattering

For high energy neutrino scattering on quarks and anti-quarks, the vector and axial contributions are the same. At very high Q^2 , where the quark parton model is valid, both the vector and axial K factors are expected to be 1.0. Therefore, high Q^2 neutrinos and antineutrino structure

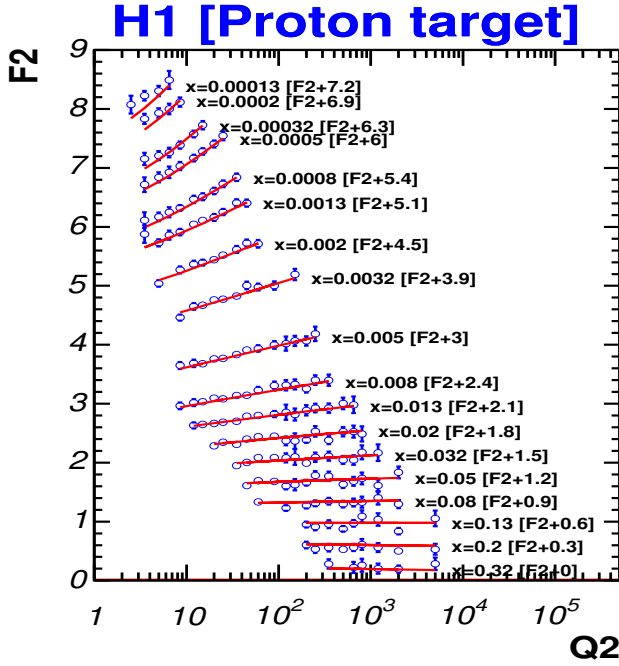


Fig. 3. The effective LO PDF model compared to charged lepton F_2 experimental data at low x from H1 (these data are included in our fit).

functions are given by :

$$\mathcal{F}_2^\nu(x, Q^2) = 2\Sigma_i [\xi_w q_i(\xi_w, Q^2) + \xi_w \bar{q}_i(\xi_w, Q^2)] .$$

and

$$x\mathcal{F}_3^\nu(x, Q^2) = 2\Sigma_i [\xi_w q_i(\xi_w, Q^2) - \xi_w \bar{q}_i(\xi_w, Q^2)] .$$

where

$$\begin{aligned} q^{\nu p} &= d + s; & \bar{q}^{\nu p} &= \bar{u} + \bar{c} \\ q^{\nu n} &= u + s; & \bar{q}^{\nu n} &= \bar{d} + \bar{c} \\ q^{\nu p} &= u + c; & \bar{q}^{\nu p} &= \bar{d} + \bar{s} \\ q^{\nu n} &= d + c; & \bar{q}^{\nu n} &= \bar{u} + \bar{s} \end{aligned} \quad (22)$$

Note that for the strangeness conserving (sc) part of the u and d quark distributions, the PDFs are multiplied by a factor of $\cos^2\theta_c$. For the strangeness non-conserving part the PDFs are multiplied by a factor of $\sin^2\theta_c$.

There are several major difference between the case of charged lepton inelastic scattering and the case of neutrino scattering. In the neutrino case we have one additional structure functions $\mathcal{F}_3^\nu(x, Q^2)$. In addition, at low Q^2 there could be a difference between the vector and axial K_i factors due a difference in the non-perturbative axial vector contributions. Unlike the vector \mathcal{F}_2 which must go to zero in the $Q^2 = 0$ limit, we expect [25,39] that the axial part of \mathcal{F}_2 can be non-zero in the $Q^2 = 0$ limit.

We already account for kinematic, dynamic higher twist and higher order QCD effects in \mathcal{F}_2 by fitting the parameters of the scaling variable ξ_w (and the K factors) to low Q^2 data for $\mathcal{F}_2^{e\mu}(x, Q^2)$. These should also be valid for the

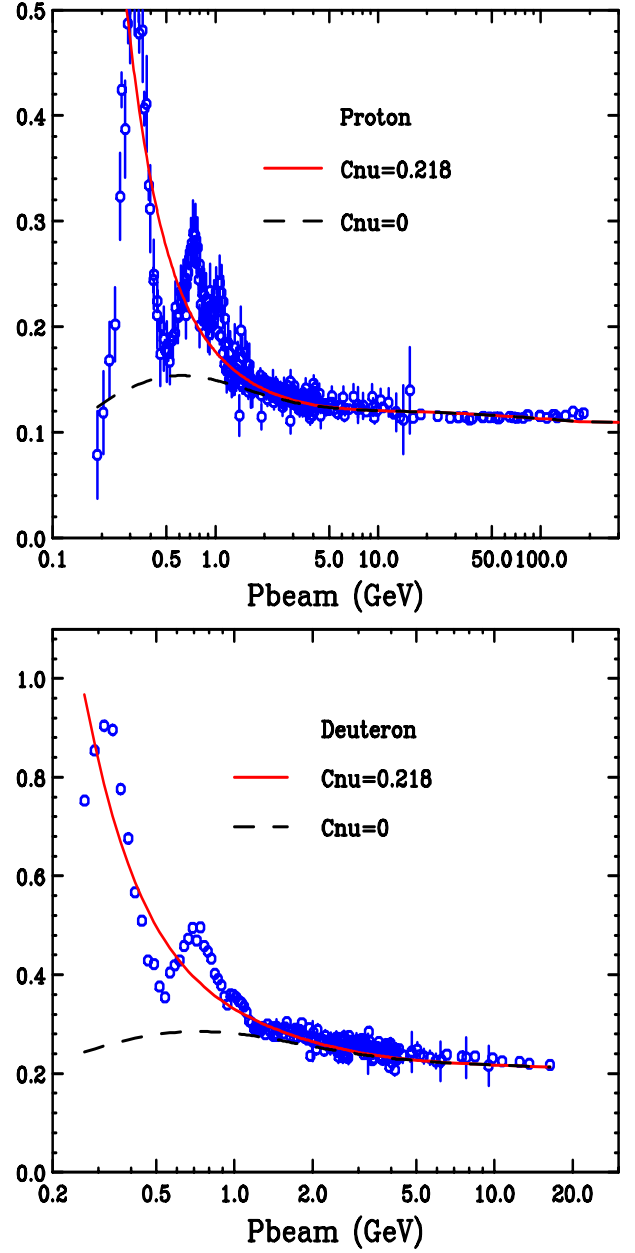


Fig. 4. The effective LO PDF model compared to photoproduction cross sections ($Q^2 = 0$ limit) at low and high energies (these data are included in our fit); [top] proton, [bot] deuteron. At very high photon energy, we include charm contribution from gluon fusion process which is needed to describe the very high energy HERA data. If we want to also describe the photo-production data in the resonance region, we need to multiply the u and d valence PDFs by $K^{LW} = (\nu^2 + C^{low-\nu})/\nu^2$. The red line includes the K^{LW} factor, and the dashed black line does not includes the K^{LW} factor.

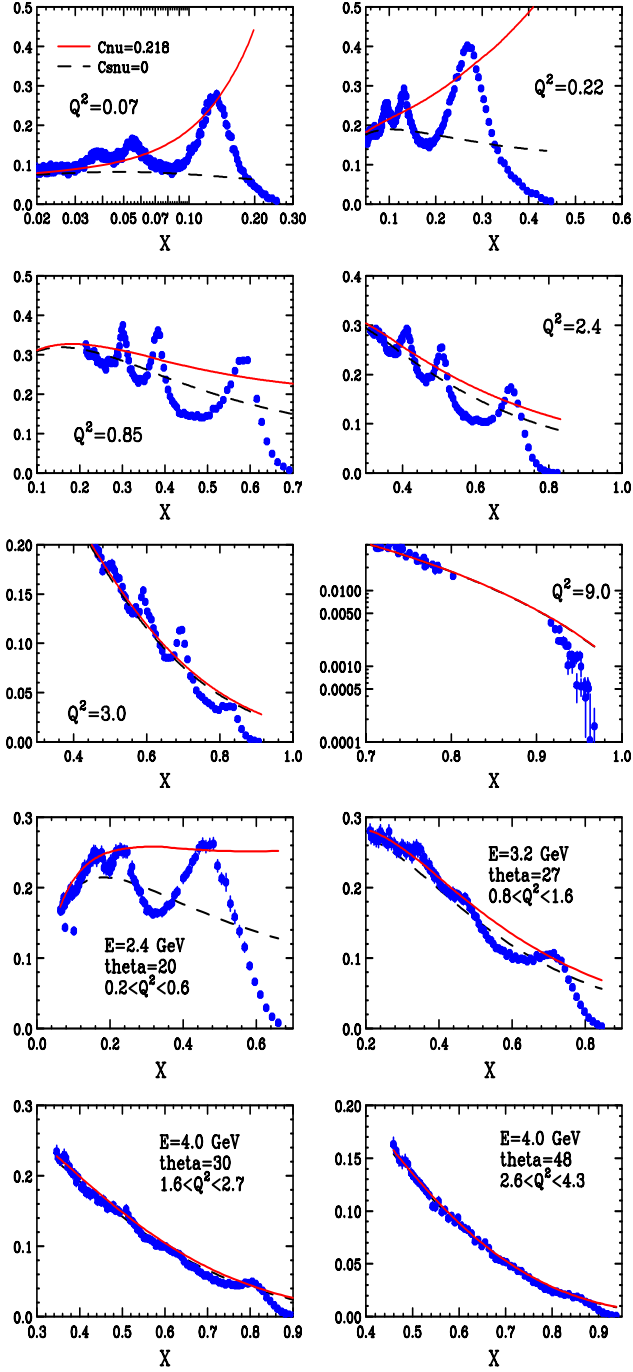


Fig. 5. Comparisons of charged lepton experimental data in the resonance region to the predictions of our effective LO model: [top] six plots to the proton data, [bot] four plots to the deuteron data. The red line includes the K^{LW} factor and the dashed black line does not include the K^{LW} factor.

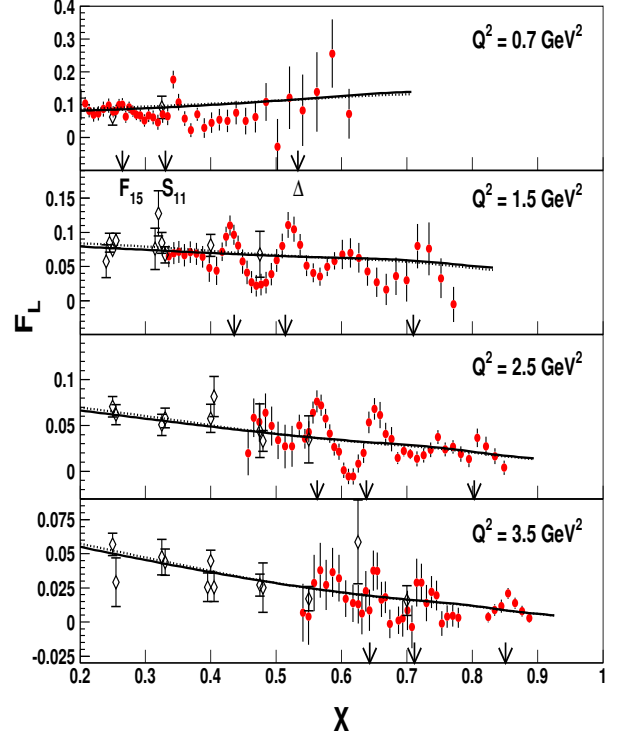


Fig. 6. Comparisons of the predictions of our model to proton data for \mathcal{F}_L (note that data for \mathcal{F}_L are not included in our fit).

vector part of \mathcal{F}_2 in neutrino scattering.

$$\mathcal{F}_2^{\nu, vector}(x, Q^2) = \Sigma_i K_i^{vector}(Q^2) \xi_w q_i(\xi_w, Q^2) + \Sigma_j K_j^{vector}(Q^2) \xi_w \bar{q}_j(\xi_w, Q^2) \quad (23)$$

However, the higher order QCD effects in \mathcal{F}_2 and $x\mathcal{F}_3$ are different. We account for the different scaling violations in \mathcal{F}_2 and $x\mathcal{F}_3$ (from higher order QCD terms) by adding a correction factor $H(x, Q^2)$ as follows.

$$x\mathcal{F}_3^\nu(x, Q^2) = 2H(x, Q^2) \left\{ \Sigma_i K_i^{vector} \xi_w q_i(\xi_w, Q^2) - \Sigma_j K_j^{vector} \xi_w \bar{q}_j(\xi_w, Q^2) \right\} \quad (24)$$

We obtain an approximate expression for $H(x, Q^2)$ as the ratio of two ratios as follows:

$$H(x, Q^2) = D_{xF_3}(x, Q^2)/D_{F_2}(x, Q^2) \quad (25)$$

where

$$D_{xF_3}(x, Q^2) = \frac{x\mathcal{F}_3^{nlo}(x, Q^2)}{x\mathcal{F}_3^{lo}(x, Q^2)} \\ D_{F_2}(x, Q^2) = \frac{\mathcal{F}_2^{nlo}(x, Q^2)}{\mathcal{F}_2^{lo}(x, Q^2)} \quad (26)$$

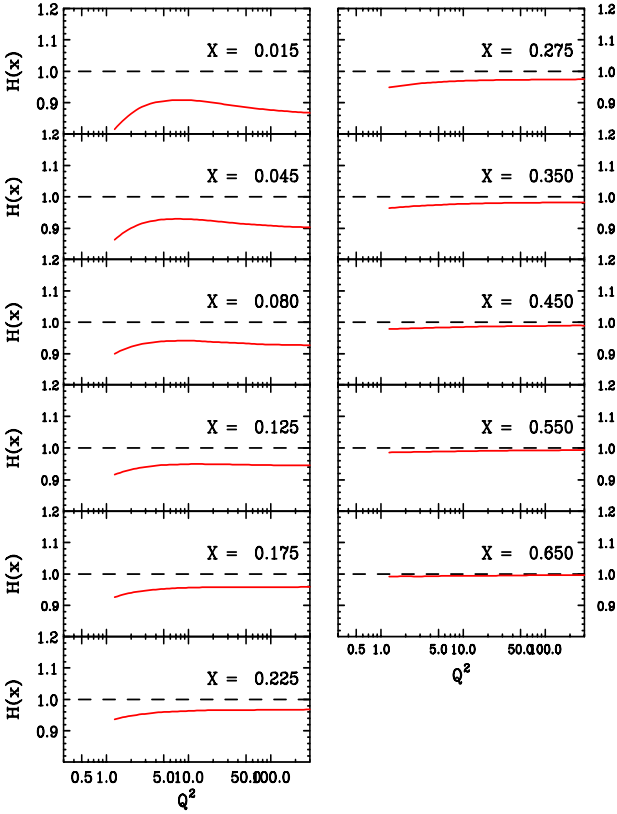


Fig. 7. The x and Q^2 dependence of the factor $H(x, Q^2)$ that accounts for the difference in the QCD higher order corrections in \mathcal{F}_2 and $x\mathcal{F}_3$

The double ratio $H(x, Q^2)$ is calculated by the TR-VFS scheme[38] with MRST991 NLO PDFs. This ratio turns out to be almost independent of Q^2 . The results of this calculation at $Q^2 = 8(\text{GeV}/c)^2$, shown in Fig 8 are fitted with the following functional form:

$$H(x, Q^2) = 0.914 + 0.296x - 0.374x^2 + 0.165x^3 \quad (27)$$

We use the above function as an approximation for $H(x, Q^2)$ for all values of Q^2 .

In our previous [11, 12] analysis we assumed $H(x, Q^2)=1$, and $K_i^{axial}(Q^2)=K_i^{vector}(Q^2)$. This assumption is valid for $Q^2 > 0.3 (\text{GeV}/c)^2$. Here, we improve our previous analysis by introducing $K_i^{axial}(Q^2)$ factors which are different from $K_i^{vector}(Q^2)$ (for the sea quarks) and include the $H(x, Q^2)$ correction for $x\mathcal{F}_3$.

7 $2x\mathcal{F}_1$ and the longitudinal structure function

In the extraction of the original GRV98 LO PDFs, no separate longitudinal contribution was included. The quark distributions were directly fit to \mathcal{F}_2 data. A full modeling of electron and muon cross section requires also a description of $2x\mathcal{F}_1$. We use a non-zero longitudinal \mathcal{R} in reconstructing $2x\mathcal{F}_1$ by using a fit of \mathcal{R} to measured data. In

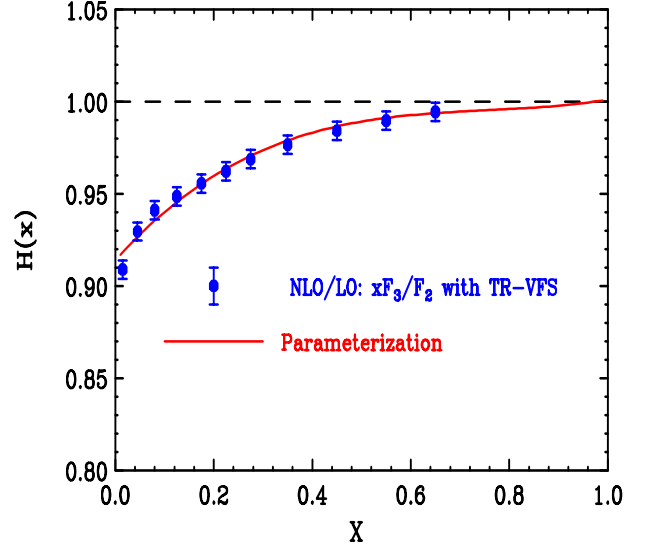


Fig. 8. A fit to the x dependence of the factor $H(x, Q^2)$ that accounts for the difference in the QCD higher order corrections in \mathcal{F}_2 and $x\mathcal{F}_3$ (at $Q^2 = 8 (\text{GeV}/c)^2$).

general, $2x\mathcal{F}_1^{e/\mu}$ is given by

$$2x\mathcal{F}_1^{e/\mu}(x, Q^2) = \mathcal{F}_2^{e/\mu}(x, Q^2) \times \frac{1 + 4M^2x^2/Q^2}{1 + \mathcal{R}(x, Q^2)}. \quad (28)$$

The \mathcal{R}_{1998} function[37] provides a good description of the world's data for \mathcal{R} in the $Q^2 > 0.30 (\text{GeV}/c)^2$ and $x > 0.05$ region (where most of the \mathcal{R} data are available).

$$\mathcal{R}_{e/\mu}(x, Q^2 > 0.3) = \mathcal{R}_{1998}(x, Q^2 > 0.3) \quad (29)$$

However, the \mathcal{R}_{1998} function breaks down. Thus, we freeze the function at $Q^2 = 0.3 (\text{GeV}/c)^2$ and introduce a K factor for \mathcal{R} in the $Q^2 < 0.3 (\text{GeV}/c)^2$ region to make a smooth transition for $\mathcal{R}_{e/\mu}$ from $Q^2 = 0.3 (\text{GeV}/c)^2$ down to $Q^2 = 0$ by forcing \mathcal{R}_{vector} to approach zero at $Q^2 = 0$, as expected in the photoproduction limit. This procedure keeps a $1/Q^2$ behavior at large Q^2 and matches to \mathcal{R}_{1998} at $Q^2 = 0.3 (\text{GeV}/c)^2$.

$$\mathcal{R}_{e/\mu}(x, Q^2 < 0.3) = 3.633 \times \frac{Q^2}{Q^4 + 1} \times \mathcal{R}_{1998}(x, Q^2 = 0.3)$$

Using the above fits to \mathcal{R} as measured in electron/muon scattering we use the following expressions for the vector part of $2x\mathcal{F}_1$ neutrino scattering.

$$\begin{aligned} 2x\mathcal{F}_1^{vector}(x, Q^2) &= \mathcal{F}_2^{vector}(x, Q^2) \times \frac{1 + 4M^2x^2/Q^2}{1 + \mathcal{R}(x, Q^2)} \\ \mathcal{R}_{vector}(x, Q^2 > 0.3) &= \mathcal{R}_{1998}(x, Q^2 > 0.3) \\ \mathcal{R}_{vector}(x, Q^2 < 0.3) &= \mathcal{R}_{e/\mu}(x, Q^2 < 0.3) \end{aligned}$$

The above expressions have the correct limit at $Q^2 = 0$.

A more recent fit to \mathcal{R} that includes updated \mathcal{R} measurements from Jefferson Lab (including resonance data) has been recently published by M.E. Christy and P.E. Bosted[40]. However, in the kinematic region of our fits the difference between the Christy-Bosted fit and the \mathcal{R}_{1998} fit is small.

8 Charm production in neutrino scattering

Neutrino scattering is not as simple as the case of charged lepton scattering because of charm production. For the non-charm production (ncp) components we use $\mathcal{F}_2^{ncp}(x, Q^2)$, $2x\mathcal{F}_1^{ncp}(x, Q^2)$ (sum of vector and axial parts) and $x\mathcal{F}_3^{ncp}(x, Q^2)$ as described above.

For the charm production components of $\mathcal{F}_2^{cp}(x, Q^2)$, $x\mathcal{F}_3^{cp}(x, Q^2)$ and $2x\mathcal{F}_1^{cp}(x, Q^2)$ the variable ξ_w now includes a non-zero $M_c = 1.32$ GeV/c².

The target mass calculations as discussed by Barbieri et. al[23] imply that $\mathcal{F}_2^{\nu-cp}$ is described by $\mathcal{F}_2^{\nu-cp}(\xi_w, Q^2)$, and the other two structure functions are multiplied by the factor $K_{charm} = \frac{Q^2}{Q^2 + M_c^2}$. Therefore, to include charm production we use the following expression for charm production processes.

$$\begin{aligned} K_{charm} &= \frac{Q^2}{Q^2 + M_c^2} \\ \mathcal{F}_2^{\nu, vector-cp}(x, Q^2) &= \Sigma_i K_i^{vector}(Q^2) \\ &\times [\xi_w q_i(\xi_w, Q^2) + \xi_w \bar{q}_i(\xi_w, Q^2)] \\ 2x\mathcal{F}_1^{\nu, cp}(x, Q^2) &= K_{charm} \\ &\times \frac{1 + 4M^2 x^2 / Q^2}{1 + \mathcal{R}(\xi_w, Q^2)} \mathcal{F}_2^{cp}(x, Q^2) \end{aligned} \quad (30)$$

and

$$\begin{aligned} x\mathcal{F}_3^{\nu}(x, Q^2) &= 2H(x, Q^2)K_{charm} \\ &\left\{ \Sigma_i K_i^{vector} \xi_w q_i(\xi_w, Q^2) \right. \\ &\left. - \Sigma_j K_j^{vector} \xi_w \bar{q}_j(\xi_w, Q^2) \right\} \end{aligned} \quad (31)$$

We use the \mathcal{R}_{1998} parametrization [20] for the vector part of \mathcal{R}^{ncp} and \mathcal{R}^{cp} .

9 Nuclear corrections

In the comparison with neutrino charged-current differential cross section on iron, a nuclear correction for iron targets should be applied. Previously, we used the following parameterized function, $f(x)$ (a fit to experimental electron and muon scattering data for the ratio of iron

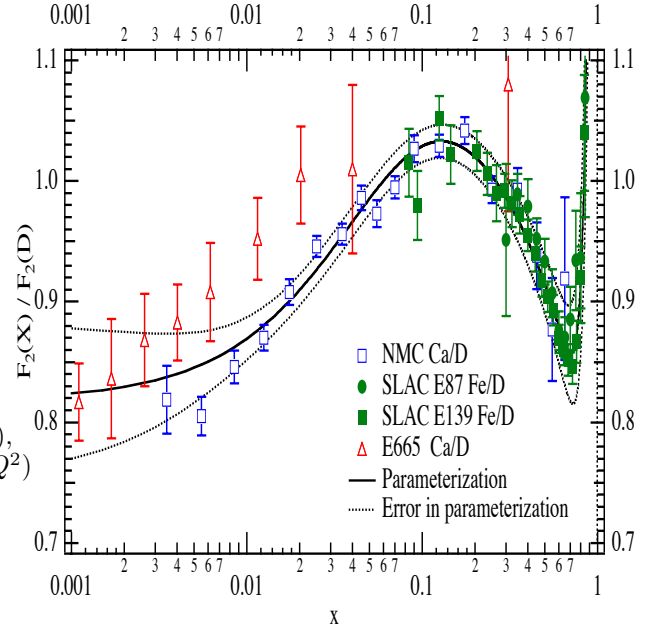


Fig. 9. The ratio of \mathcal{F}_2 data for heavy nuclear targets and deuterium as measured in charged lepton scattering experiments (SLAC, NMC, E665). The band shows the uncertainty of the parametrized curve (as a function of x) from the statistical and systematic errors in the experimental data [41].

to deuterium cross sections, shown in Fig 9), to convert deuterium structure functions to (isoscalar) iron structure functions [41];

$$\begin{aligned} \mathcal{F}(x) = (Fe/D) &= 1.096 - 0.364 x \\ &- 0.278 e^{-21.94 x} + 2.772 x^{14.417} \end{aligned} \quad (32)$$

However, we find that the ratio of iron to deuterium structure function measurements at SLAC and Jefferson Lab are better described in terms of the target mass variable ξ_{TM} . If ξ_{TM} is used, then the function that describes the iron to deuterium ratios in the deep inelastic region is also valid in the resonance region. Therefore, we use the following updated function $\mathcal{F}_{updated}(\xi_{TM})$.

$$\begin{aligned} \mathcal{F}_{updated}(\xi_{TM}) = (Fe/D) &= 1.096 - 0.38 \xi_{TM} \\ &- 0.3 e^{-23\xi_{TM}} + 8 \xi_{TM}^{15} \end{aligned} \quad (33)$$

Figure 10 shows a comparison of Jefferson lab measurements of the ratio of electron scattering cross sections on iron to deuterium in the resonance region[42] to data from SLAC E87[43], SLAC E139[44], and SLAC E140[45] and NMC[47] in the deep inelastic region. The data are plotted versus ξ_{TM} and are compared to our updated fit function $\mathcal{F}_{updated}(\xi_{TM})$. For comparison we also show the ratios as measured in photoproduction[33].

For the ratio of deuterium cross sections to cross sections on free nucleons we use the following function obtained from a fit to SLAC data on the nuclear dependence of electron scattering cross sections [19].

$$\begin{aligned} f(x) &= 0.985 \times (1 + 0.422x - 2.745x^2 \\ &+ 7.570x^3 - 10.335x^4 + 5.422x^5). \end{aligned} \quad (34)$$

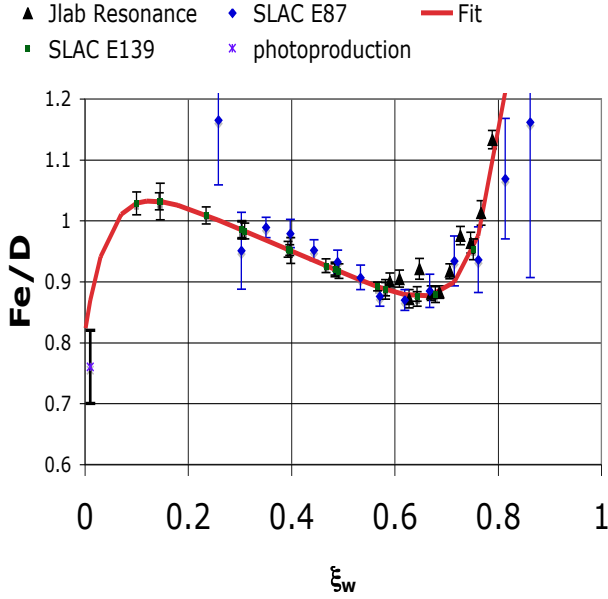


Fig. 10. The ratio of \mathcal{F}_2 data of iron (Fe) and deuterium as measured in charged lepton scattering experiments in the deep inelastic region (SLAC E87, SLAC E139, SLAC E140) as compared to Jlab data in the resonance region as a function of the target mass variable ξ_{TM} . Also shown is $\mathcal{F}_{updated}(\xi_{TM})$, which is a revised fit of Fe/D as measured in charged lepton scattering data as a function of ξ_{TM} . We also show the ratios as measured in photoproduction[33] at $\xi_{TM} = 0$.

This correction shown in Fig. 11 is only valid in the $0.05 < x < 0.75$ region.

Figures 12 show the measured ratio of structure functions for gold (Au)[45] or lead (Pb)[47] to the structure functions for iron (Fe) versus ξ_{TM} . Figure 13 shows the ratio of the structure functions for iron to the structure functions for carbon versus ξ_{TM} .

The gold (and lead) data are described by the function $\frac{\mathcal{F}_{Au,Pb}}{\mathcal{F}_{Fe}}(\xi_{TM}) = 0.932 + 2.461 \xi - 24.23 \xi_{TM}^2 + 101.03 \xi_{TM}^3 - 203.47 \xi_{TM}^4 + 193.85 \xi_{TM}^5 - 69.82 \xi_{TM}^6$.

The carbon data[45,46] are described by the function $\frac{\mathcal{F}_{Fe}}{\mathcal{F}_C}(\xi_{TM}) = 0.919 + 1.844 \xi_{TM} - 12.73 \xi_{TM}^2 + 36.89 \xi_{TM}^3 - 46.77 \xi_{TM}^4 + 21.22 \xi_{TM}^5$.

In neutrino scattering, we assume that the nuclear correction factor for \mathcal{F}_2 , $x\mathcal{F}_3$ and $2x\mathcal{F}_1$ are the same. This is a source of systematic error because the nuclear shadowing corrections at low x can be different for the vector and axial structure functions. This difference can be accounted for by assuming a specific theoretical model[39].

10 d/u correction

The d/u correction for the GRV98 LO PDFs is obtained from the NMC data for $\mathcal{F}_2^D/\mathcal{F}_2^P$. Here, Eq. 34 is used to remove nuclear binding effects in the NMC deuterium \mathcal{F}_2 data. The correction term, $\delta(d/u)$ is obtained by keeping

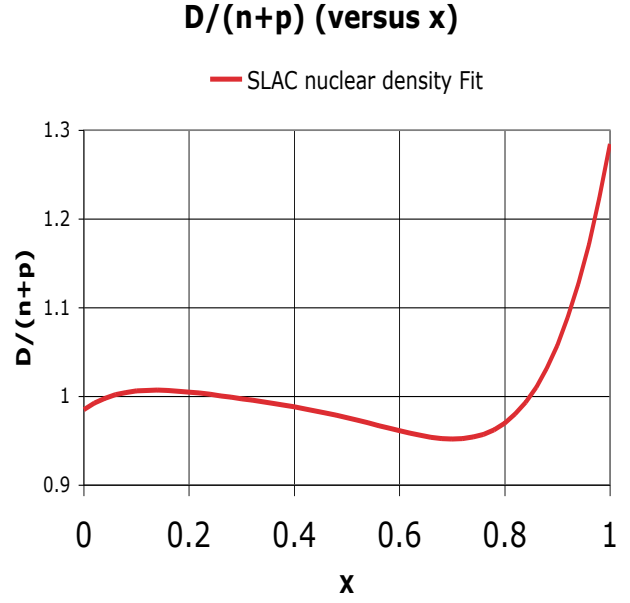


Fig. 11. The total correction for nuclear effects (binding and Fermi motion) in the deuteron, $\mathcal{F}_2^d/\mathcal{F}_2^{n+p}$, as a function of x , extracted from fits to the nuclear dependence of SLAC \mathcal{F}_2 electron scattering data. This correction is only valid in the $0.05 < x < 0.75$ region.

the total valence and sea quarks the same.

$$\delta(d/u)(x) = -0.00817 + 0.0506x + 0.0798x^2, \quad (35)$$

where the corrected d/u ratio is $(d/u)' = (d/u) + \delta(d/u)$. Thus, the modified u and d valence distributions are given by

$$u'_v = \frac{u_v}{1 + \delta(d/u) \frac{u_v}{u_v + d_v}} \quad (36)$$

$$d'_v = \frac{d_v + u_v \delta(d/u)}{1 + \delta(d/u) \frac{u_v}{u_v + d_v}}. \quad (37)$$

The same formalism is applied to the modified u and d sea distributions. We find that the modified u and d sea distributions (based on NMC data) also agree with the NUSEA data in the range of x between 0.1 and 0.4. Thus, we find that corrections to u and d sea distributions are not necessary.

11 Axial structure functions \mathcal{F}_2 , and $2x\mathcal{F}_1$

At $Q^2 = 0$ the vector structure function $\mathcal{F}_2^{\nu-vector}$ is required to go to zero. In contrast, the axial structure function $\mathcal{F}_2^{\nu-axial}$ is not constrained to go to zero at $Q^2 = 0$. At higher Q^2 the vector and axial structure functions should be equal. Since the contribution of the structure function $2x\mathcal{F}_1$ to the cross section near $Q^2 = 0$ is very small we set

$$2x\mathcal{F}_1^{\nu-axial}(x, Q^2) = 2x\mathcal{F}_1^{\nu-vector}(x, Q^2)$$

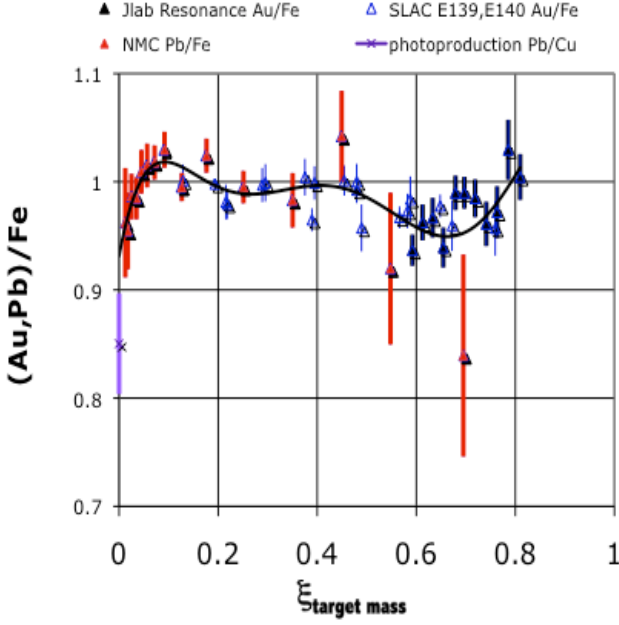


Fig. 12. The ratio of \mathcal{F}_2 data for gold (Au) to \mathcal{F}_2 data for Iron (Fe) as measured in charged lepton scattering experiments in the deep inelastic region (SLAC E139, SLAC E140) as compared to Jlab data in the resonance region versus the target mass variable ξ_{TM} . Also shown is the ratio of \mathcal{F}_2 data for lead (Pb) to \mathcal{F}_2 data for iron (Fe) from the NMC collaboration. For comparison we also show the ratio of lead to copper cross sections (Pb/Cu) as measured in photoproduction[33].

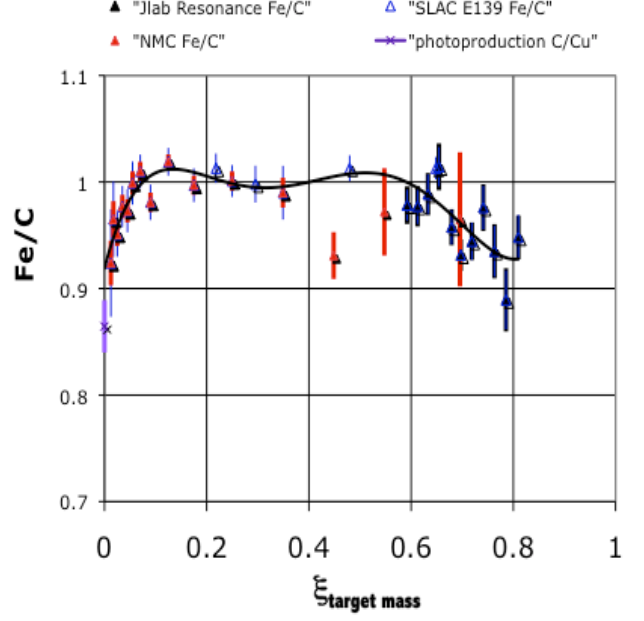


Fig. 13. The ratio of \mathcal{F}_2 data for carbon (C) to \mathcal{F}_2 data for iron (Fe) as measured in charged lepton scattering in the deep inelastic region (SLAC E139) as compared to Jlab data in the resonance region versus the target mass variable ξ_{TM} . Also shown is the ratio of \mathcal{F}_2 data for carbon to \mathcal{F}_2 data for iron from the NMC collaboration. For comparison we also show the ratio of carbon to copper cross sections (C/Cu) as measured in photoproduction[33].

We compare neutrino data to two types of variations of our model

11.1 Bodek-Yang Model Type I

The first variation of our model (which we refer to as type I) assumes that the vector and axial components of the structure function \mathcal{F}_2^ν are equal at all values of Q^2 . i.e.

$$\mathcal{F}_2^{\nu-axial}(x, Q^2) = \mathcal{F}_2^{\nu-vector}(x, Q^2) \text{ (type I)}$$

11.2 Bodek-Yang model Type II

In the second variation of our model we account for the fact that the axial and vector structure functions are not equal at $Q^2=0$ as follows:

$$\begin{aligned} \mathcal{F}_2^{\nu-axial}(x, Q^2) = & \Sigma_i K_i^{axial}(Q^2) \xi_w q_i(\xi_w, Q^2) \\ & + \Sigma_j K_j^{axial}(Q^2) \xi_w \bar{q}_j(\xi_w, Q^2) \end{aligned} \quad (38)$$

11.2.1 Axial sea

For sea quarks, use the same axial K factor for all types of quarks.

$$K_{sea}^{axial}(Q^2) = \frac{Q^2 + P_{sea}^{axial} C_{sea}^{axial}}{Q^2 + C_{sea}^{axial}}$$

We refer to the non-zero value of the K_{sea}^{axial} at $Q^2=0$ as the PCAC term in \mathcal{F}_2 . We use $P_{sea}^{axial} = 0.018 \pm 0.09$, and $C_{sea}^{axial} = 0.3$. With the above values we get:

$$K_{sea}^{axial}(Q^2) = \frac{Q^2 + 0.018 \pm 0.09}{Q^2 + 0.3}$$

which implies that the axial K factor for the sea at $Q^2 = 0$ is 0.06. The axial sea parameters are extracted from low Q^2 CCFR and CHORUS data, and from PCAC considerations as follows:

- For an iron target (assuming a nuclear shadowing ratio $Fe/D = 0.8$) the value of $P_{sea}^{axial} = 0.6$ yields $\mathcal{F}_2^{axial}(\xi_w = 0.00001, Q^2 = 0)_{Fe} = 0.25 \pm 0.11$, which is close to the value of 0.210 ± 0.02 measured by CCFR [26] using a different functional form for the extrapolation of neutrino data to $Q^2 = 0$.
- For a deuteron target the value of $P_{sea}^{axial} = 0.6$ yields $\mathcal{F}_2^{axial}(\xi_w = 0.00001, Q^2 = 0)_{(p+n)/2} = 0.33 \pm 0.16$ for the average of the neutron and proton structure

functions, which is close to the value calculated from PCAC in the model of Kulagin and Peti[39].

- The value of $C_{sea}^{axial} = 0.3$ is chosen because it yields a PCAC contribution $\mathcal{F}_2^{axial}(\xi_w = 0.00001, Q^2 = 1) = 0.08$, which is close to the value calculated in the model of Kulagin and Peti[39] at $Q^2=1$ (GeV/c)².

11.2.2 Axial valence

For the valence quarks, we note that the following is a good approximation to the vector K factor.

$$K_{valence}^{vector}(Q^2) \approx [1 - G_D^2(Q^2)] \approx \frac{Q^2}{Q^2 + 0.18}$$

We use a similar form for the axial K factor for valence quarks.

$$K_{valence}^{axial}(Q^2) = \frac{Q^2 + P_{valence}^{axial}}{Q^2 + 0.18} \text{ (type II)}$$

Where $P_{valence}^{axial} = 0.018 \pm 0.09$ is chosen to get agreement with measured high energy neutrino and antineutrino total cross sections. Therefore,

$$K_{valence}^{axial}(Q^2) = \frac{Q^2 + 0.018 \pm 0.09}{Q^2 + 0.18} \text{ (type II)}$$

which implies that the axial K factor for the valence quarks at $Q^2 = 0$ is 0.1.

We use the same axial K factor for the u and d valence quarks.

As mentioned earlier, we assume $2x\mathcal{F}_1^{axial} = 2x\mathcal{F}_1^{vector}$. This is because the non-zero PCAC component of \mathcal{F}_2^{axial} at low Q^2 is purely longitudinal and therefore does not contribute to $2x\mathcal{F}_1^{axial}$ which is purely transverse.

12 Comparison to Neutrino Data on Heavy Targets

We now compare the predictions of our model to neutrino data on lead (CHORUS [52]) and iron (CCFR [19, 50]). In these comparison we assume that the ratio of the structure functions on a nucleus to the structure functions on free nucleons for neutrinos is the same as measured in electron/muon scattering for \mathcal{F}_2 .

We assume that the nuclear correction factors are the same for the axial and vector part of the structure functions. This is a source of systematic error because the nuclear shadowing corrections at low x can be different for the vector and axial terms (this difference can be only be accounted for by assuming a specific theoretical model[39]).

The published CHORUS and CCFR data have been corrected for radiative corrections. In addition, the CHORUS data have been corrected for the neutron excess in lead. Therefore, we compare the CHORUS data to our model for an isoscalar target.

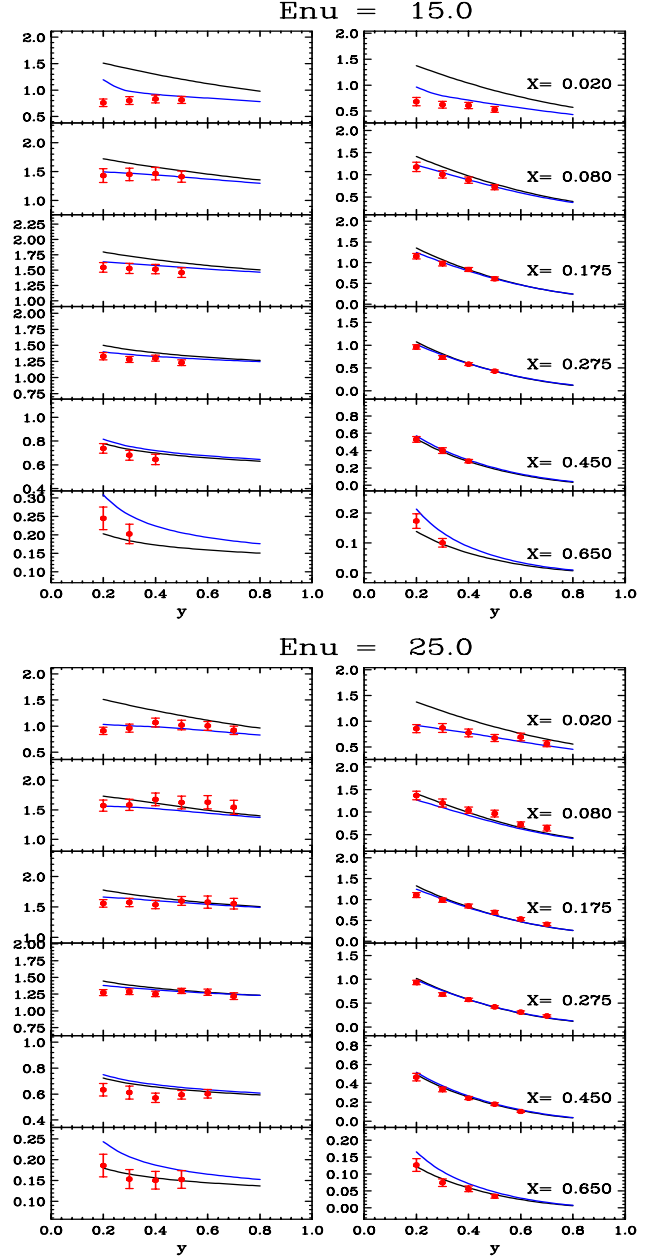


Fig. 14. The ratio of charged-current neutrino and antineutrino differential cross sections $d^2\sigma/dxdy$ on lead from CHORUS [52] to our default model which includes a non zero PCAC contribution to the sea quarks at low Q^2 (BY Type II). The ratios are shown for energies of 15 and 25 GeV . On the left side we show the comparison for neutrino cross sections and on the right side we show the prediction for antineutrinos. The blue line is the ratio of a modified version of the model for which the axial structure functions are set equal to the vector structure functions (BY Type I) to the default model which includes the non zero PCAC axial contribution to the sea quarks at low Q^2 (BY Type II). The CHORUS and CCFR data favor the BY Type II default model.

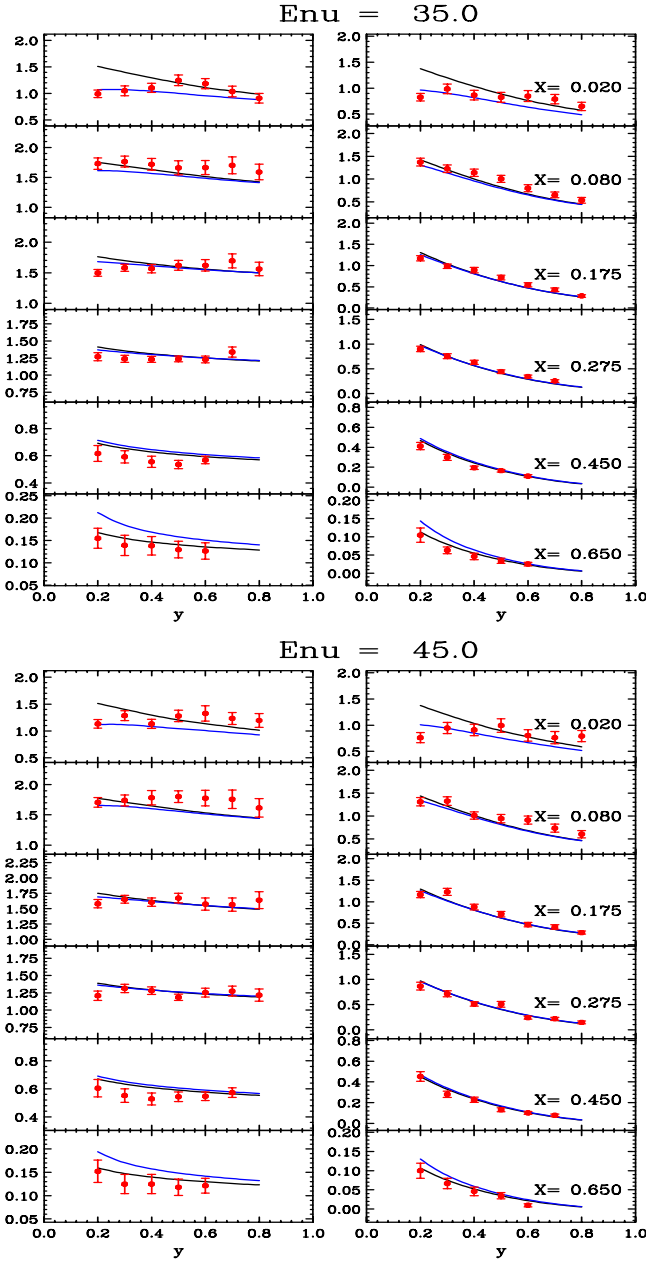


Fig. 15. The ratio of charged-current neutrino and antineutrino differential cross sections $d^2\sigma/dxdy$ on lead from CHORUS [52] (blue points) and CCFR cross sections (red points) on iron [19, 50] to our default model which includes a non zero PCAC contribution to the sea quarks at low Q^2 (BY Type II). The ratios are shown for energies of 35 and 45 GeV . On the left side we show the comparison for neutrino cross sections and on the right side we show the prediction for antineutrinos. The blue line is the ratio of the predictions from a modified version of the model for which the axial structure functions are set equal to the vector structure functions (BY Type I), to to the predictions from the default model (BY Type II). The CHORUS and CCFR data for at this lower energies data favor the BY Type II default model. The CHORUS and CCFR data favor the BY Type II default model.

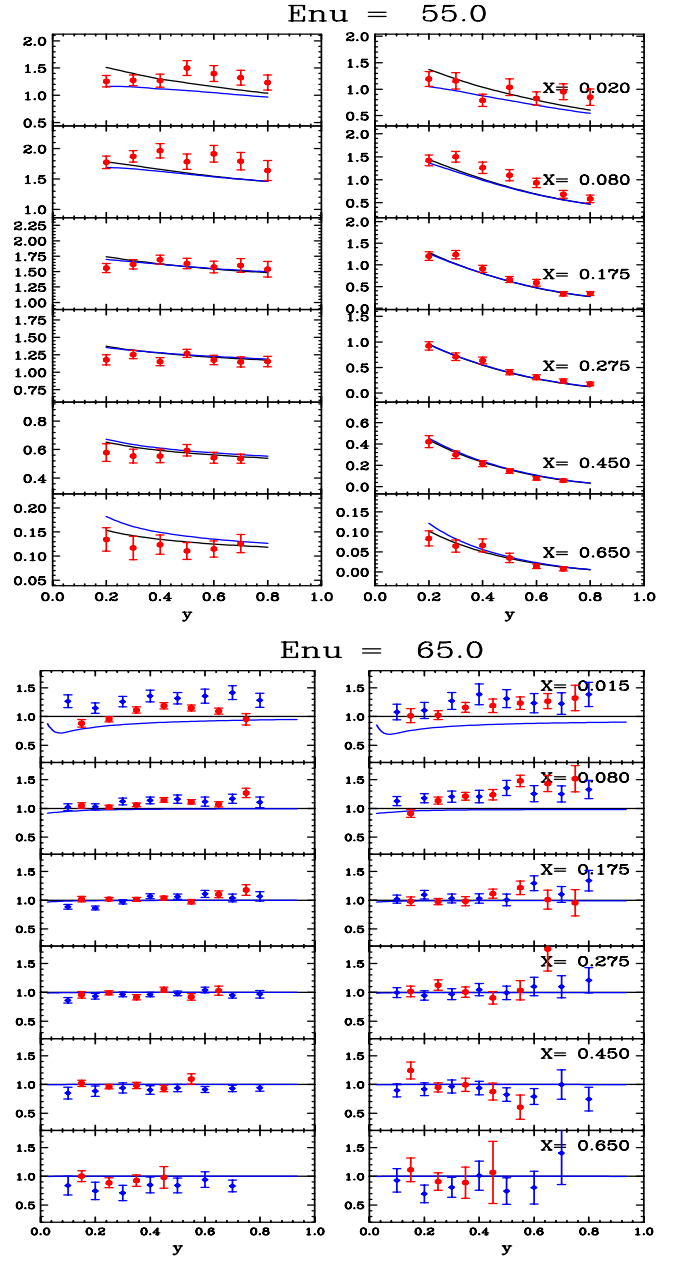


Fig. 16. Same as Fig.15 for energies of 55 and 65 GeV .

Figures 14- 16 show the ratio of charged-current neutrino and antineutrino differential cross sections $d^2\sigma/dxdy$ on lead from CHORUS (blue points) and CCFR cross sections on iron (red points), to our default model. We refer to the default model, which includes a non zero PCAC contribution to the sea quarks at low Q^2 as BY Type II. The ratios are shown for neutrino energies of 15, 25, 35, 45, 55 and 65 GeV . On the left side we show the comparison for neutrinos and on the right side we show the prediction for antineutrinos. The blue line is the ratio of the predictions from a modified version of the model for which the axial structure functions are set equal to the vector structure functions (referred to as BY Type I), to to the predictions from the default model (BY Type II).

The CHORUS and CCFR data at the lower energies favor the default model (BY Type II). Comparisons to CHORUS and CCFR data at higher energies are presented in an Appendix.

13 Neutrino and Antineutrino Total Cross Sections

Figure 17 shows our prediction for the total neutrino and antineutrino cross sections per nucleon for an iron isoscalar target. The top part of the figure shows our prediction for σ_ν/E , the middle part shows our prediction for $\sigma_{\bar{\nu}}/E$, and the bottom of the figure shows the prediction for the ratio $\sigma_{\bar{\nu}}/\sigma_\nu$ as a function of energy.

In the calculation of the total cross sections, the contribution of the $W > 1.4 \text{ GeV}$ region is calculated from our model for nucleons bound in an isoscalar iron target. The contribution of the $\Delta(1232)$ ($1.1 < W < 1.4 \text{ GeV}$) region is calculated from the GENIE monte Carlo (on free nucleons), and the contribution of the quasielastic peak is calculated using BBA2008 form factors (on free nucleons) as shown in Fig. 18.

The red lines are the prediction of our default model which includes a non zero PCAC contribution to the sea quarks at low Q^2 (BY Type II). The black lines are the prediction of a modified version of the model for which the axial structure functions are set equal to the vector structure functions (BY Type I). The blue lines are the average [3] of the all of the world's data for energies between 30 and 50 GeV on an isoscalar iron target of $\sigma_\nu/E = 0.675 \times 10^{-38} \text{ cm}^2/\text{GeV}$ and $\sigma_{\bar{\nu}}/E = 0.329 \times 10^{-38} \text{ cm}^2/\text{GeV}$.

At an energy of 40 GeV, the default version (BY Type II) of our model yields $\sigma_\nu/E = 0.673 \times 10^{-38} \text{ cm}^2/\text{GeV}$ which is within 0.3% of the world average value of $0.675 \times 10^{-38} \text{ cm}^2/\text{GeV}$, and $\sigma_{\bar{\nu}}/E = 0.316 \times 10^{-38} \text{ cm}^2/\text{GeV}$ which is within 4% of the world average value of $0.329 \times 10^{-38} \text{ cm}^2/\text{GeV}$. At 40 GeV the ratio of the neutrino to antineutrino cross sections predicted by our model is $\sigma_{\bar{\nu}}/\sigma_\nu = 0.470$, which is within 3.7% of the world average of 0.4874 for energies between 30 and 50 GeV. At 40 GeV neutrino energy, the largest contribution to the total cross section comes from the $W > 1.8 \text{ GeV}$ region, with smaller contributions from resonance production and quasielastic scattering. Therefore, comparisons of the predicted total cross section to experimental data in this region provide a good test of our model.

At energies lower than 30 GeV, the sum of the contributions of the $1.4 < W < 1.8 \text{ GeV}$ resonance region, the $1.1 < W < 1.4 \text{ GeV}$ $\Delta(1232)$ region and quasielastic scattering is more significant. At the lower energies, we suggest that our model be used for $W > 1.8 \text{ GeV}$, and be matched to other models of resonance production and quasielastic scattering. Since our model provides a reasonable description of the $1.4 < W < 1.8 \text{ GeV}$ region, this matching should be continuous.

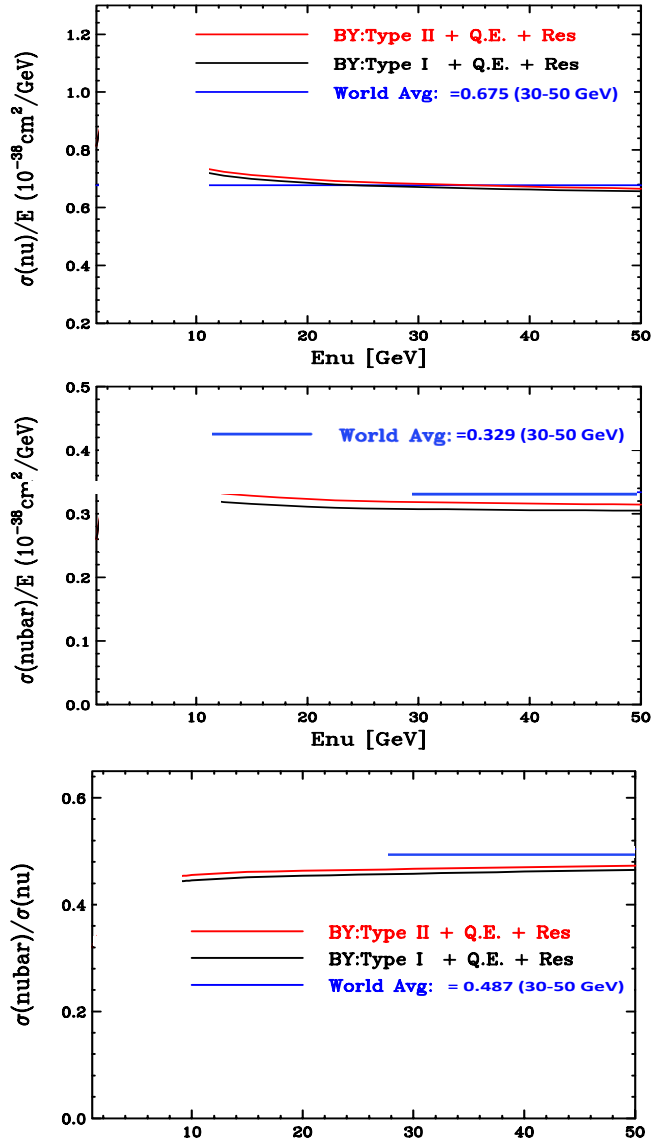


Fig. 17. Model predictions for σ_ν/E per nucleon in units of $10^{-38} \text{ cm}^2/\text{GeV}$ (top), $\sigma_{\bar{\nu}}/E$ per nucleon in units of $10^{-38} \text{ cm}^2/\text{GeV}$ (middle), and the ratio $\sigma_{\bar{\nu}}/\sigma_\nu$ (bottom) as a function of energy. The red lines are the prediction of our default model which includes a non zero PCAC contribution to the sea quarks at low Q^2 (BY Type II). The black lines are the prediction of a modified version of the model for which the axial structure functions are set equal to the vector structure functions (BY Type I). The blue lines are the averages [3] of all of the world's data for energies between 30 and 50 GeV ($\sigma_\nu/E = 0.675 \times 10^{-38} \text{ cm}^2/\text{GeV}$, $\sigma_{\bar{\nu}}/E = 0.329 \times 10^{-38} \text{ cm}^2/\text{GeV}$ and $\sigma_{\bar{\nu}}/\sigma_\nu = 0.484$). The contribution of the $W > 1.4 \text{ GeV}$ region is calculated from our model for nucleons bound in an iron target. The contribution of the $1.1 < W < 1.4 \text{ GeV}$ region is calculated from the GENIE monte Carlo, and the contribution of quasielastic peak is calculated using BBA2008 form factors.

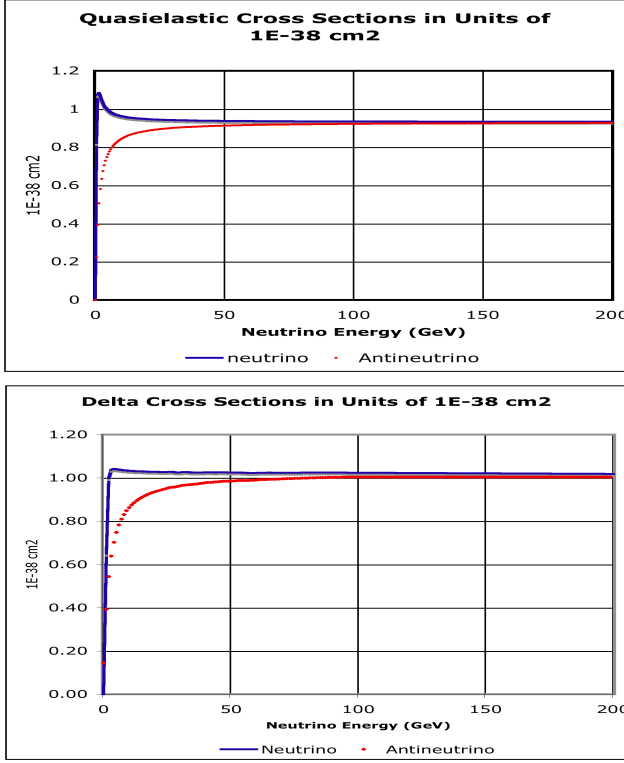


Fig. 18. Top: Quasielastic neutrino-neutron (blue) and antineutrino-proton (red) cross sections (on free nucleons) versus neutrino energy calculated with BBBA2008 form factor. Bottom: The sum the cross sections for the production of the $\Delta(1232)$ resonance on neutrons and protons (neutrinos in blue and antineutrinos in red) from the GENIE Monte Carlo.

14 Systematic errors in the application of the model

The model predicts neutrino cross sections at the Born level. Therefore, radiative corrections must be applied to the model if it is compared to non-radiatively corrected neutrino or charged lepton scattering data. In general, all published charged lepton scattering data are radiatively corrected. Similarly, published neutrino differential cross sections (e.g. CCFR, CDHSW, CHORUS, NuTeV) are radiatively corrected, and therefore can be directly compared to the model.

The model describes all inelastic charged lepton scattering data and photoproduction on hydrogen and deuterium for $W > 1.8 \text{ GeV}/c^2$ at all values of Q^2 (and gives a reasonable average cross section in the resonance region for $W > 1.4 \text{ GeV}/c^2$). Therefore, under the assumption of CVC, the model describes the vector part of the cross section in neutrino scattering very well. The modeling of the axial structure functions at low Q^2 has larger uncertainties.

The total cross sections for neutrino (anti-neutrino) can be approximately expressed in terms of (on average) the fraction antiquarks $f_{\bar{q}} = \bar{Q}/(Q + \bar{Q})$ in the nucleon, and (on average) the ratio of longitudinal to transverse

Table 3. Sources of systematic error in the predicted inelastic contribution to the total cross section on iron (for $W > 1.8 \text{ GeV}$). The change (positive or negative) in the neutrino, antineutrino and the $\sigma_{\bar{\nu}}/\sigma_{\nu}$ ratio that originate from a plus one standard deviation change in the ratio of transverse to longitudinal structure functions (R), the fraction of antiquarks ($f_{\bar{q}}$), the axial quark-antiquark sea, and the overall normalization of the structure functions (N).

source	change (error)	change in σ_{ν}	change in $\sigma_{\bar{\nu}}$	change in $\sigma_{\bar{\nu}}/\sigma_{\nu}$
R	-0.05	+1.0%	+2.0%	+1%
$f_{\bar{q}}$	+5%	-0.7%	+1.4%	+2.1%
P (K^{axial})	+ 50%	+1.3%	+1.9%	+1.2%
N	+3%	+3%	+3%	0
Total		$\pm 3.4\%$	$\pm 4.3\%$	$\pm 2.5\%$

cross sections \mathcal{R} as follows:

$$\sigma(\nu N) \approx \frac{G_F^2 ME}{\pi} (Q + \bar{Q}) \left[(1 - f_{\bar{q}}) + \frac{1}{3} f_{\bar{q}} - \frac{1}{6} \mathcal{R} \right], \quad (39)$$

and

$$\sigma(\bar{\nu} N) \approx \frac{G_F^2 ME}{\pi} (Q + \bar{Q}) \left[\frac{1}{3} (1 - f_{\bar{q}}) + f_{\bar{q}} - \frac{1}{6} \mathcal{R} \right], \quad (40)$$

With $\langle \mathcal{R} \rangle = 0.2$ and $\langle f_{\bar{q}} \rangle = 0.1725$, we obtain $\langle \sigma_{\bar{\nu}}/\sigma_{\nu} \rangle = 0.487$, which is the world's experimental average value in the 30-50 GeV energy range. The above expressions are used to estimate the systematic error in the cross section originating from uncertainties in \mathcal{R} and $f_{\bar{q}}$ (as shown in Table 3).

We estimate the total systematic error in the modeling of the cross sections on iron for the $W > 1.8 \text{ GeV}/c^2$ region to be $\pm 3.4\%$ for neutrinos, $\pm 4.3\%$ for antineutrinos, and $\pm 2.5\%$ in the $\sigma_{\bar{\nu}}/\sigma_{\nu}$ ratio (for neutrino energies below 50 GeV).

The following sources contribute to the systematic error.

- Longitudinal structure function: In our analysis we use the \mathcal{R}_{1998} parametrization. We assign an error of ± 0.05 in the value of \mathcal{R} to account for the fact that preliminary results from the JUPITER Jefferson Lab collaboration indicates that \mathcal{R} for heavy nucleus is smaller by 0.03-0.04 than R for deuterium. This error can be reduced when more precise low Q^2 data on $\mathcal{R}(x, Q^2)$ from the JUPITER collaboration (for hydrogen, deuterium, and heavy nuclei) is published.
- The antiquark fraction in the nucleon ($f_{\bar{q}}$). We estimate an uncertainty of $\pm 10\%$ in the fraction of the sea quarks at low Q^2 .
- We assign a $\pm 3\%$ error in the overall normalization of the structure functions (N) on iron, partly from the error in normalization of the SLAC data on deuterium and partly from the level of consistency of the Fe/D cross section ratio among the various measurement as seen in Fig.10.
- Axial K factors for sea and valence quarks: We assume a 50% error on P_{sea}^{axial} and $P_{valence}^{axial}$.

- Charm sea: Since the GRV98 PDFs do not include a charm sea, the charm sea contribution must be added separately. This can be implemented either by using a boson-gluon fusion model, or by incorporating a charm sea from another set of PDFs. We modeled the contribution of the charm sea using a photon-gluon fusion model when we compared our predictions to photoproduction data at HERA. If the charm sea contribution is neglected, the model underestimates the cross section at very high neutrino energies in the low x and large ν region. At neutrino energies less than 50 GeV, the charm sea contribution is very small and can be neglected.

The following are additional sources of systematic errors which could be constrained when new low energy cross sections from MINERvA becomes available.

- Nuclear corrections: In our comparisons to neutrino scattering on heavy targets, we assume that the nuclear corrections are the same for the three structure functions. We also assume that the corrections are the same for the axial and vector contributions (and are equal to the nuclear corrections for F_2 as measured in charged lepton scattering). We also assume that the nuclear corrections are only a function of ξ_{TM} and are independent of Q^2 . In general, nuclear corrections can be different for sea and valence quarks, and also for the longitudinal and transverse structure functions. Some of the systematic error can be reduced when Jefferson Lab data on the nuclear dependence of $\mathcal{R} = \sigma_L/\sigma_T$ is published (expected in 2011). Other systematic errors in the nuclear corrections can be reduced by either using specific theoretical models[39] to account for the differences in the nuclear corrections between neutrino and charged lepton scattering (as a function of Q^2 and x for various nuclear targets), or when MINERvA data on the nuclear dependence of neutrino structure functions becomes available.

15 Appendix: Comparison to CHORUS and CCFR data at very high energies

Figures 19- 24 show ratio of charged-current neutrino and antineutrino differential cross sections $d^2\sigma/dxdy$ on lead from CHORUS [52] (blue points) and CCFR cross sections on iron [19,50] to our default model which includes a non zero PCAC contribution to the sea quarks at low values of Q^2 (BY Type II). The ratios are shown for energies of 75, 85, 110, 130, 150, 170, 190, 215, 245, 275, 304 and 340 GeV. On the left side we show the comparison for neutrino cross sections and on the right side we show the prediction for antineutrinos. The blue line is the ratio of a modified version of the model for which the axial structure functions are set equal to the vector structure functions (BY Type I) to to the default model which includes the non zero PCAC axial contribution to the sea quarks at low Q^2 (BY Type II).

The CHORUS and CCFR data at these higher energies are in also agreement with the BY Type II model,

except at the lowest value of x . We expect deviations at high neutrino energies at the lowest values of x and high ν because the charm sea is not included in the model. In addition, in this region the nuclear corrections for neutrinos may be different from the corrections measured in electron/muon experiments. Our model has been primarily used[14–16] at low energies, where the contribution of the charm sea is negligible. We find that our model also describes the differential cross sections measurements of CDHSW [51].

16 Appendix -Results with GRV94 PDFs and

x_w

For completeness we describe our earlier analysis [11,12] in which we used another modified scaling variable [27] x_w with GRV94 PDFs (instead of GRV98) and simplified K factors. In that analysis we modified the leading order GRV94 PDFs as follows:

1. We increased the d/u ratio at high x as previously described [17].
2. Instead of the scaling variable x we used the scaling variable $x_w = (Q^2 + B)/(2M\nu + A)$ (or $=x(Q^2 + B)/(Q^2 + Ax)$). This modification was used in early fits to SLAC data [28]. The parameter A provides for an approximate way to include *both* target mass and higher twist effects at high x , and the parameter B allows the fit to be used all the way down to the photoproduction limit ($Q^2=0$).
3. In addition as was done in earlier non-QCD based fits [25,26] to low energy data, we multiplied all PDFs by a factor $K=Q^2 / (Q^2 + C)$. This was done in order for the fits to describe low Q^2 data in the photoproduction limit, where \mathcal{F}_2 is related to the photoproduction cross section.
4. Finally, we froze the evolution of the GRV94 PDFs at a value of $Q^2 = 0.24$ (for $Q^2 < 0.24$), because GRV94 PDFs are only valid down to $Q^2 = 0.23$ (GeV/c)².

As was done for GRV98, in the GRV94 analysis, the measured structure functions were also corrected for the BCDMS systematic error shift[21] and for the relative normalizations between the SLAC, BCDMS and NMC data [17,18]. The deuterium data were corrected for nuclear binding effects [17,18]. A simultaneous fit to both proton and deuteron SLAC, NMC and BCDMS data (with $x > 0.07$ only) yields $A=1.735$, $B=0.624$ and $C=0.188$ (GeV/c)² with GRV94 LO PDFs ($\chi^2 = 1351/958$ DOF). Note that for x_w the parameter A accounts for *both* target mass and higher twist effects.

In our studies with GRV94 PDFs we used the earlier \mathcal{R}_{world} fit [20] for \mathcal{R}^{ncp} and \mathcal{R}^{cp} . \mathcal{R}_{world} is parameterized by:

$$\mathcal{R}_{world}(x, Q^2 > 0.35) = \frac{0.0635}{\log(Q^2/0.04)}\theta(x, Q^2) + \frac{0.5747}{Q^2} - \frac{0.3534}{Q^4 + 0.09}, \quad (41)$$

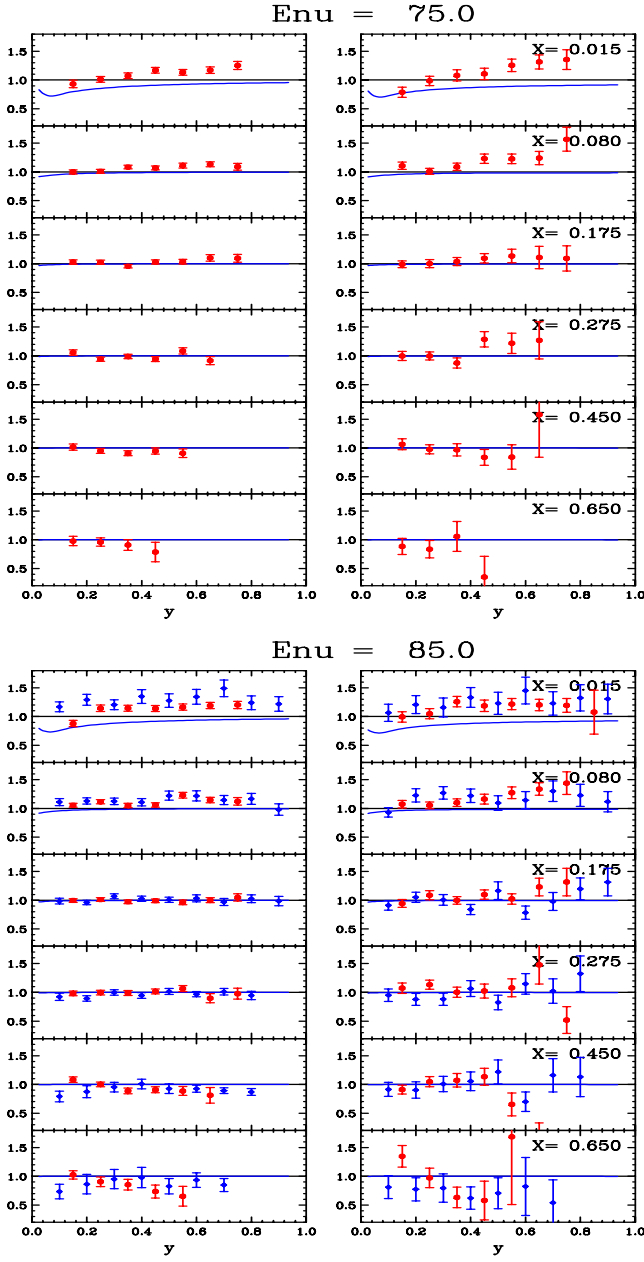


Fig. 19. The ratio of charged-current neutrino and antineutrino differential cross sections $d^2\sigma/dx dy$ on lead from CHORUS [52] (blue points) and CCFR cross sections (red points) on iron [19, 50] to our default model which includes a non zero PCAC contribution to the sea quarks at low Q^2 (BY Type II). The ratios are shown for energies of 75 and 85 GeV. On the left side we show the comparison for neutrino cross sections and on the right side we show the prediction for antineutrinos. The blue line is the ratio of a modified version of the model for which the axial structure functions are set equal to the vector structure functions (BY Type I) to the default model which includes the non zero PCAC axial contribution to the sea quarks at low Q^2 (BY Type II). We expect deviations at high neutrino energies at the lowest values of x and high ν because the charm sea is not included in the model. In addition, in this region the nuclear corrections for neutrinos may be different from the corrections measured in electron/muon experiments.

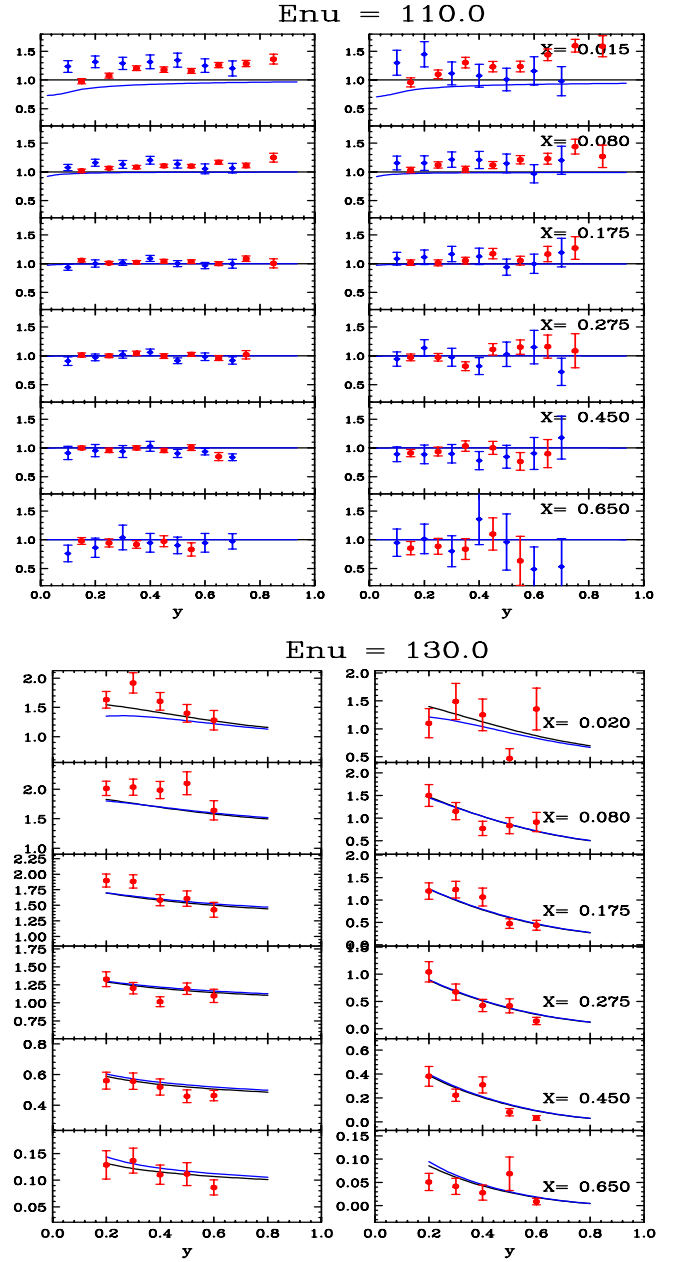


Fig. 20. Same as Fig.19 for energies of 110 and 130 GeV.

where $\theta = 1 + \frac{12Q^2}{Q^2+1.0} \times \frac{0.125^2}{0.125^2+x^2}$. The \mathcal{R}_{world} function provided a good description of the world's data for \mathcal{R} at that time in the $Q^2 > 0.35$ (GeV/c^2) and $x > 0.05$ region (where most of the \mathcal{R} data are available). However, for electron and muon scattering and for the vector part of neutrino scattering the \mathcal{R}_{world} function breaks down below $Q^2 = 0.35$ (GeV/c^2). Therefore, we freeze the function at $Q^2 = 0.35$ (GeV/c^2). For electron and muon scattering and for the vector part of \mathcal{F}_1 we introduce a K factor for \mathcal{R} in the $Q^2 < 0.35$ (GeV/c^2) region. The new function provides a smooth transition for the vector \mathcal{R} (we use $\mathcal{R}_{vector} = \mathcal{R}_{e/\mu}$) from $Q^2 = 0.35$ (GeV/c^2) down to $Q^2 = 0$ by forcing \mathcal{R}_{vector} to approach zero at $Q^2 = 0$ as expected

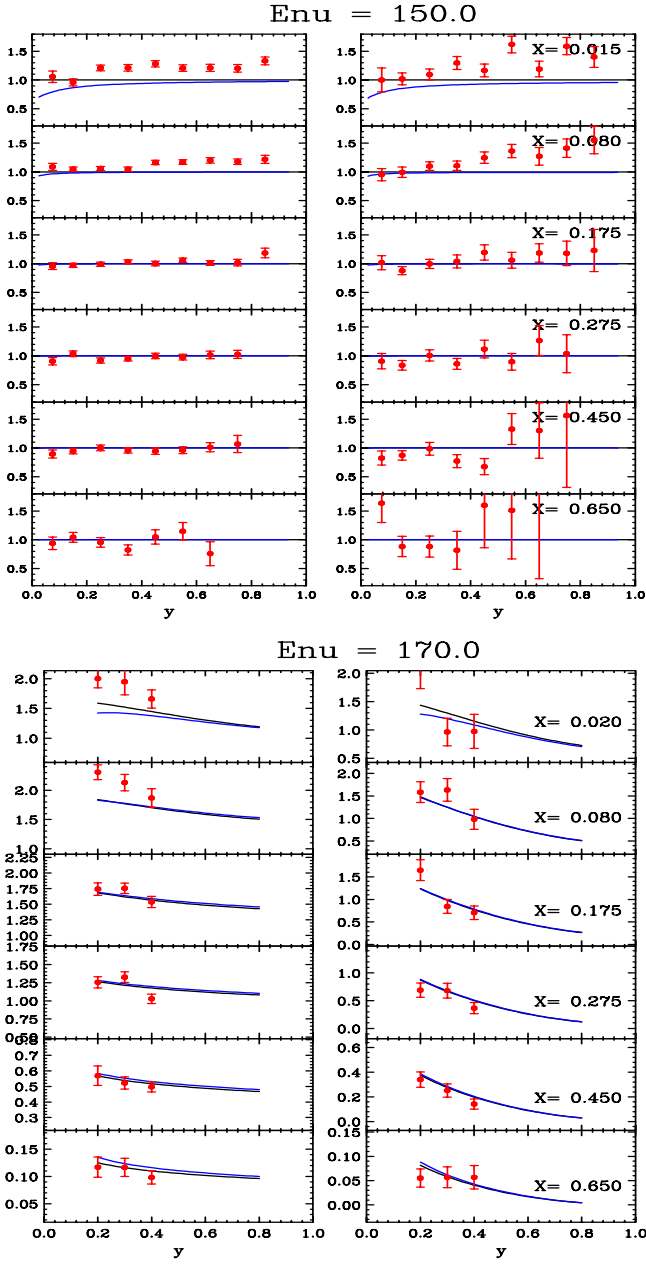


Fig. 21. Same as Fig.19 for energies of 150 and 170 GeV.

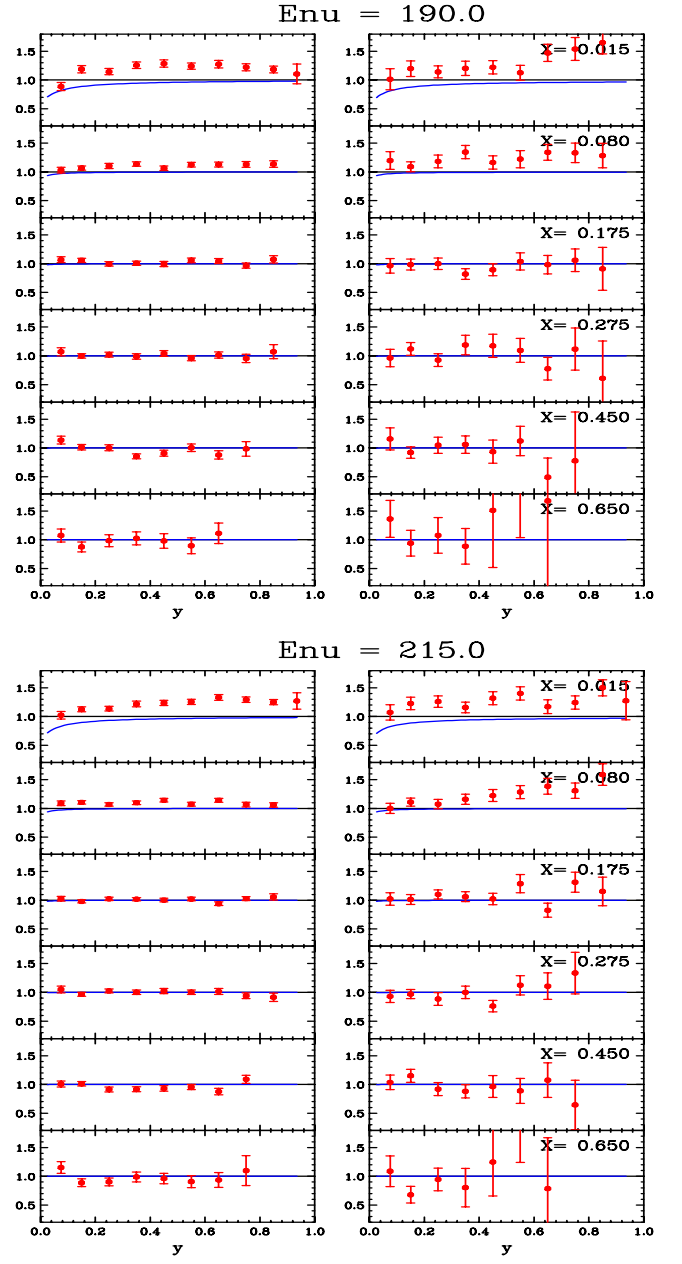


Fig. 22. Same as Fig.19 for energies of 190 and 215 GeV.

in the photoproduction limit (while keeping a $1/Q^2$ behavior at large Q^2 and matching to \mathcal{R}_{world} at $Q^2 = 0.35$ (GeV/c) 2).

$$\mathcal{R}_{vector}(x, Q^2 < 0.35) = 3.207 \times \frac{Q^2}{Q^4 + 1} \times \mathcal{R}_{world}(x, Q^2 = 0.35).$$

17 Appendix: The Adler sum rule

The Adler sum rules are derived from current algebra and are therefore valid at all values of Q^2 . The equations below are for *strangeness conserving*(sc) processes.

The Adler sum rules for the vector part of the structure function $\mathcal{W}_2^{\nu-vector}$ is given by:

$$|F_V(Q^2)|^2 + \int_{\nu_0}^{\infty} \mathcal{W}_{2n-sc}^{\nu-vector}(\nu, Q^2) d\nu - \int_{\nu_0}^{\infty} \mathcal{W}_{2p-sc}^{\nu-vector}(\nu, Q^2) d\nu = 1 \quad (42)$$

Where the limits of the integrals are from pion threshold ν_0 where $W = M_\pi + M_P$ to $\nu = \infty$. At $Q^2 = 0$, the inelastic part of $\mathcal{W}_2^{\nu-vector}$ goes to zero, and the sum rule is saturated by the quasielastic contribution $|F_V(Q^2)|^2$.

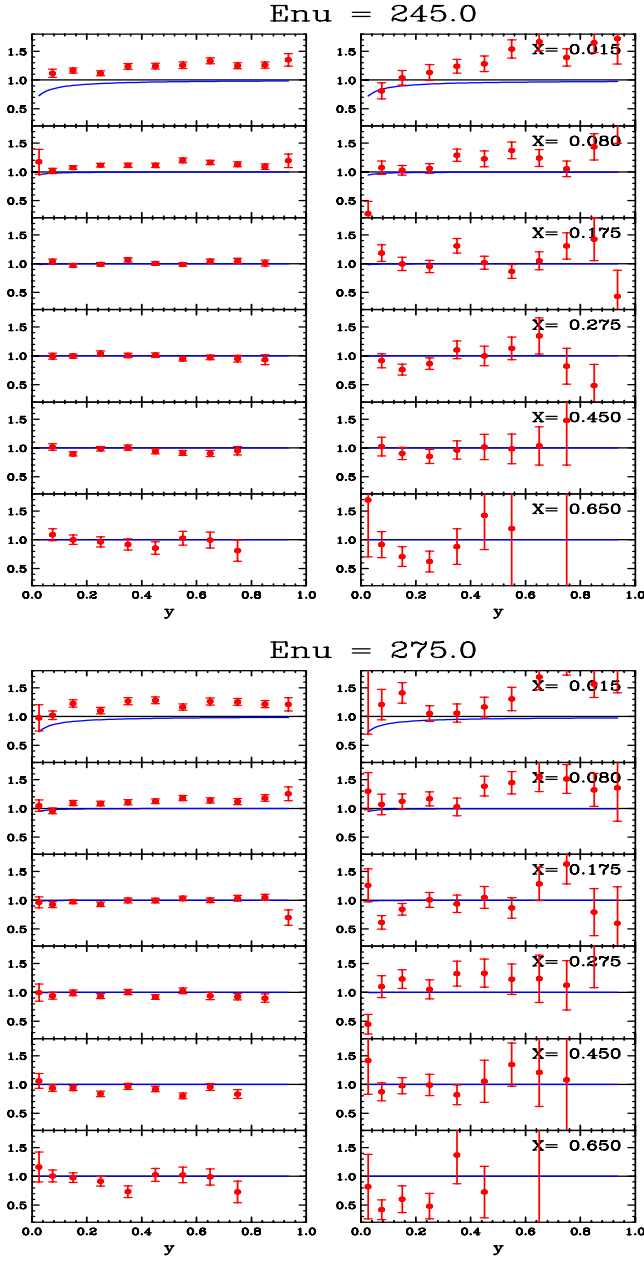


Fig. 23. TSame as Fig.19 for energies of 245 and 275 GeV.

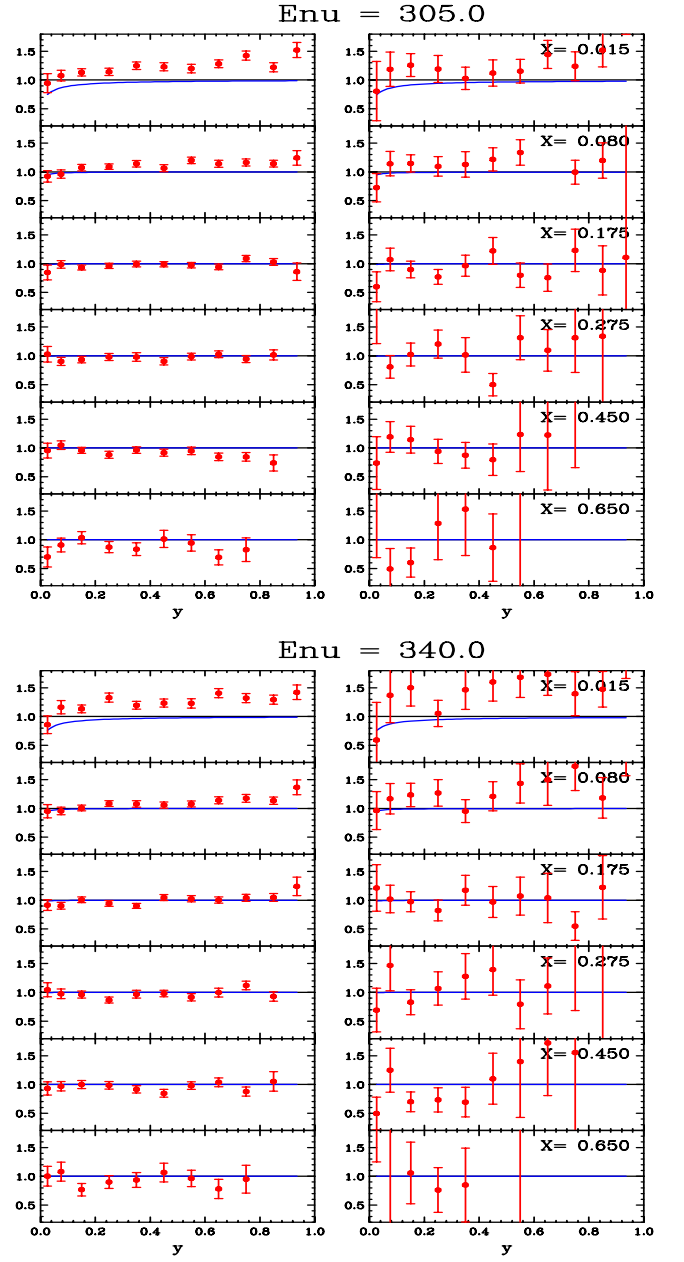


Fig. 24. Same as Fig.19 for energies of 305 and 340 GeV.

Here $= Q^2/(4M^2)$, and

$$|F_V(Q^2)|^2 = \frac{[G_E^V(Q^2)]^2 + \tau[G_M^V(Q^2)]^2}{1 + \tau},$$

In the dipole approximation we have

$$G_E^V(Q^2) = G_E^P(Q^2) - G_E^N(Q^2) \approx G_D(Q^2)$$

$$G_M^V(Q^2) = G_M^P(Q^2) - G_M^N(Q^2) \approx 4.706 G_D(Q^2)$$

$$G_D = 1/(1 + Q^2/M_V^2)^2$$

Where $M_V^2 = 0.71 \text{ (GeV/c)}^2$. Note that in all of our calculations, we do not use the dipole approximation (we use BBBA2008 [48] vector and axial form factors).

The Adler sum rule for $\mathcal{W}_2^{\nu-axial}$ is given by:

$$|\mathcal{F}_A(Q^2)|^2 + \int_{\nu_0}^{\infty} \mathcal{W}_{2n-sc}^{\nu-axial}(\nu, Q^2) d\nu - \int_{\nu_0}^{\infty} \mathcal{W}_{2p-sc}^{\nu-axial}(\nu, Q^2) d\nu = 1$$

where in the dipole approximation

$$\mathcal{F}_A \approx -1.267/(1 + Q^2/M_A^2)^2$$

and $M_A = 1.014 \text{ GeV/c}^2$ from reference[48].

The Adler sum rule for $\mathcal{W}_1^{\nu-vector}$ is given by:

$$\tau |G_M^V(Q^2)|^2 + \int_{\nu_0}^{\infty} \mathcal{W}_{1n}^{\nu-vector}(\nu, Q^2) d\nu - \int_{\nu_0}^{\infty} \mathcal{W}_{1p}^{\nu-vector}(\nu, Q^2) d\nu = 1 \quad (43)$$

The Adler sum rule for $\mathcal{W}_1^{\nu-axial}$ is given by:

$$(1 + \tau) |\mathcal{F}_A(Q^2)|^2 + \int_{\nu_0}^{\infty} \mathcal{W}_{1n-sc}^{\nu-axial}(\nu, Q^2) d\nu - \int_{\nu_0}^{\infty} \mathcal{W}_{1p-sc}^{\nu-axial}(\nu, Q^2) d\nu = 1 \quad (44)$$

The Adler sum rule for \mathcal{W}_3^{ν} is given by:

$$2\mathcal{F}_A(Q^2)G_M^V(Q^2) + \int_{\nu_0}^{\infty} \mathcal{W}_{3n-sc}^{\nu}(\nu, Q^2) d\nu - \int_{\nu_0}^{\infty} \mathcal{W}_{3p-sc}^{\nu}(\nu, Q^2) d\nu = 0 \quad (45)$$

We use the Alder sum rule for $\mathcal{W}_2^{\nu-vector}$ to constrain the form of the $K_{valence}^{vector}(Q^2)$ factor for $\mathcal{W}_2^{\nu-vector}$. At low Q^2 we approximate $|F_V(Q^2)|^2$ by $G_D^2(Q^2)$, and use the following K factors for $\mathcal{W}_2^{\nu-vector}$.

$$K_{valence}^{vector}(Q^2) = [1 - G_D^2(Q^2)] \times \left(\frac{Q^2 + C_{v2}}{Q^2 + C_{v1}} \right) \quad (46)$$

where the values of the parameters C_{v2d} , C_{v1d} , C_{v2u} and C_{v1u} are obtained from a fit to the charged lepton scattering and photoproduction data. With this $K_{valence}^{vector}(Q^2)$ factor, the Adler sum rule for $\mathcal{W}_2^{\nu-vector}$ is then approximately satisfied. At $Q^2 = 0$, the inelastic part of $\mathcal{W}_2^{\nu-vector}$ goes to zero, and the sum rule is saturated by the quasielastic contribution.

Note that the contribution of the $\Delta(1232)$ resonance to the Adler sum rule is negative. Near $Q^2 = 0$ the $\Delta(1232)$ contribution is small in the vector case (since it must be zero at $Q^2 = 0$) and can be neglected. However, for the axial case the contribution of the $\Delta(1232)$ at $Q^2 = 0$ is large and negative and cannot be neglected.

References

1. S. Fukuda *et al.*, Phys. Rev. Lett. **85**, 3999 (2000); T. Toshito, hep-ex/0105023.
2. D.G. Michael *et al.*(MINOS), Phys. Rev. Lett. **97**, 191801 (2006); <http://www-nucl.fnl.gov/Minos/>
3. P. Adamson *et al.*(MINOS), Phys. Rev. D **81**, 072002 (2010).
4. <http://www-nova.fnl.gov/>
5. M. H. Ahn *et al.*(K2K), Phys. Rev. D **74**, 072003 (2006); <http://neutrino.kek.jp/>
6. Y. Ashie *et al.*(SuperK), Phys. Rev. D **71**, 112005 (2005);
7. Y. Itow *et al.*(T2K), arXiv:hep-ex/0106019; <http://www-nova.fnl.gov/>
8. A. A. Aguilar-Arevalo *et al.*(MiniBooNE), Phys. Rev. Lett. **98**, 231801(2007)
9. Y. Nakjima *et al.*, (SciBoonE) arXiv:hep-ex/1011.213
10. <http://minerva.fnl.gov/>
11. A. Bodek and U.K. Yang (NUINT01), hep-ex/0203009, Nucl. Phys. Proc. Suppl. **112**, 70 (2002)
12. A. Bodek and U. K. Yang, (NUINT02) hep-ex/0308007.
13. Y. Hayato, Nucl Phys. Proc. Suppl. **112**, 171 (2002)
14. C.Andreopoulos (GENIE), Nucl. Instrum. Meth. A614, 87 (2010)
15. H. Gallagher (NEUGEN), Nucl. Phys. Proc. Suppl. **112** (2002)
16. D. Casper (NUANCE) , Nucl. Phys. Proc. Suppl. **112**, 161 (2002); <http://nuint.ps.uci.edu/nuance/>
17. U. K. Yang and A. Bodek, Phys. Rev. Lett. **82**, 2467 (1999)
18. U. K. Yang and A. Bodek, Eur. Phys. J. **C13**, 241 (2000)
19. U. K. Yang, Ph.D. thesis, Univ. of Rochester, UR-1583 (2001) <http://hep.uchicago.edu/~ukyang/neutrino/thesis.ps>.
20. L. W. Whitlow *et al.* (SLAC-MIT), Phys. Lett. **B282**, 433 (1995)
21. A. C. Benvenuti *et al.* (BCDMS), Phys. Lett. **B237**, 592 (1990); M. Virchaux and A. Milsztajn, Phys. Lett. B **274**, 221 (1992)
22. M. Arneodo *et al.* (NMC), Nucl. Phys. **B483**, 3 (1997)
23. H. Georgi and H. D. Politzer, Phys. Rev. **D14**, 1829 (1976); R. Barbieri *et al.*, Phys. Lett. **B64**, 171 (1976), and Nucl. Phys. **B117**, 50 (1976); J. Pestieau and J. Urias, Phys.Rev.**D8**, 1552 (1973)
24. M. Gluck, E. Reya, A. Vogt, Eur. Phys. J **C5**, 461 (1998).
25. A. Donnachie and P. V. Landshoff, Z. Phys. C **61**, 139 (1994).
26. B. T. Fleming *et al.*(CCFR), Phys. Rev. Lett. **86**, 5430 (2001).
27. F. W. Brasse *et al.*, Nucl. Phys. B **839**, 421 (1972).
28. A. Bodek *et al.*, Phys. Rev. **D20**, 1471 (1979).
29. S. Stein *et al.*, Phys. Rev. **D12**, 1884 (1975); K. Gottfried, Phys. Rev. Lett. **18**, 1174 (1967).
30. S. Adler, Phys. Rev. **143**, 1144 (1966); F. Gillman, Phys. Rev. **167**, 1365 (1968).
31. O. Lalakulich, W. Melnitchouk, and E. A. Paschos, Phys. Rev. C **75**:015202 (2007).
32. C. Adloff *et al.* (H1) , Eur Phys J C30, 32 (2003); <http://www-h1.desy.de/>
33. Photoproduction: David O. Caldwell, *et al.* Phys. Rev. Lett. **25**, 609 (1970); T.A. Armstrong *et al.* Nucl. Phys. **B41**, 445 (1972); T.A. Armstrong *et al.* Phys. Rev. **D5**, 1640 (1972); David O. Caldwell, *et al.* Phys. Rev. **D7**, 1362 (1973) (nuclear targets); David O. Caldwell *et al.* Phys. Rev. Lett. **40**, 1222, (1978); S. Chekanov *et al.* (ZEUS) Nucl. Phys. **B627**, 3 (2002); T. Ahmed *et al.* (H1) Phys. Lett. **B299** 374 (1993).
34. C. Keppel, Proc. of the Workshop on Exclusive Processes at High P_T , Newport News, VA, May (2002).
35. E. D. Bloom and F. J. Gilman, Phys. Rev. Lett. **25**, 1140 (1970).
36. Y. Liang *et al.*(E94-110), arXiv:nucl-ex/0410027.
37. K. Abe *et al.*, Phys. Lett. **B452**, 194 (1999)
38. R.S. Thorne and R.G. Roberts, Phys. Lett. B **421**, 303 (1998); Eur. Phys. J. C **19**, 339 (2001).

39. S. A. Kulagin and R. Pett, Phys. Rev. D **76**, 094023 (2007),
ibid Nucl. Phys. A **765**, 26 (2006).
40. P.E. Bosted and M.E. Christy, Phys. Rev. C **77**,
065206 (2008); M.E. Christy and P.E. Bosted,
arXiv:0712.373. Fortran program for R is available at
<http://www.jlab.org/christy/csfits/F1F209.f>.
41. W. G. Seligman, Ph.D. thesis, (CCFR) Columbia Univ.,
Nevis reports 292 (1997).
42. J. Arrington et al (Jefferson Lab), Phys.Rev. C **73**, 035205
(2006).
43. A. Bodek *et al.* (E87), Phys. Rev. Lett. 50, 1431 (1983).
44. J. Gomez *et al.* (E139, Phys. Rev. D **49**, 4348 (1994).
45. S. Dasu *et al.* (E140) , Phys. Rev. Lett. 60, 2591 (1988);
S. Dasu *et al.* (E140) Phys. Rev. D **49**, 5641 (1994).
46. R. Seely *et al.* (Jefferson Lab data on Carbon), Phys. Rev.
Lett. 103, 202301 (2009).
47. M. Arneodo (NMC) *et al.*, Nucl. Phys. B **481**, 3 (1966).
48. A. Bodek, S. Avvakumov, R. Bradford, and H. Budd, Eur.
Phys. J. C **53**, 349 (2008).
49. S. Kretzer and M. H. Reno, Phys. Rev. D **66**, 113007
(2002); Yu Seon Jeong, M.H. Reno, Phys. Rev. D **82**
033010,2010.
50. U. K. Yang *et al.*(CCFR), Phys. Rev. Lett. **87**, 251802
(2001).
51. P. Berge *et al.* (CDHSW), Zeit. Phys. C **49**, 607 (1991).
52. R. Oldeman, Proc. of 30th International Conference on
High-Energy Physics (ICHEP 2000), Osaka, Japan, 2000.
53. Q. Wu *et al.*(NOMAD), Phys. Lett. B **60**, 19 (2008).
54. C. H. Llewellyn Smith, Phys. Rep. 3C (1972); E. A.
Paschos, Electroweak Theory, Cambridge University Press
(2007).
55. F.M. Steffens and K. Tsushima , Phys. Rev. D **70**, 094040
(2004)